UCRL-ID-141663

The $^{239}Pu(n,2n)^{238}Pu$ Cross Section Inferred from IDA Calculations and GEANIE Measurements

H. Chen, W.E. Ormand, F.S. Dietrich

September 1, 2000

U.S. Department of Energy

Lawrence
Livermore
National
Laboratory

DISCLAIMER

This work was performed under the auspices of the U. S. Department of Energy by the University of California, Lawrence Livermore National Laboratory under Contract No. W-7405-Eng-48.

The ^{239}Pu(n,2n)^{238}Pu Cross Section Inferred from IDA Calculations and GEANIE Measurements

H. Chen, W.E. Ormand, and F.S. Dietrich

September 1, 2000

Lawrence Livermore National Laboratory

Abstract

This report presents the latest ^{239}Pu(n,2n)^{238}Pu cross sections inferred from calculations performed with the nuclear reaction-modeling code system, IDA, coupled with experimental measurements of partial γ-ray cross sections for incident neutron energies ranging from 5.68 to 17.18 MeV. It is found that the inferred ^{239}Pu(n,2n)^{238}Pu cross section peaks at $E_{\rm inc} \approx 11.4$ MeV with a peak value of approximately 326 mb. At $E_{\rm inc} \approx 14$ MeV, the inferred ^{239}Pu(n,2n)^{238}Pu cross section is found to be in good agreement with previous radio-chemical measurements by Lougheed. However, the shape of the inferred ^{239}Pu(n,2n)^{238}Pu cross section differs significantly from previous evaluations of ENDL, ENDF/B-V and ENDF/B-VI. In our calculations, direct, preequilibrium, and compound reactions are included. Also considered in the modeling are fission and γ-cascade processes in addition to particle emission. The main components of physics adopted and the parameters used in our calculations are discussed. Good agreement of the inferred ^{239}Pu(n,2n)^{238}Pu cross sections derived separately from IDA and GNASH calculations is shown. The two inferences provide an estimate of variations in the deduced ^{239}Pu(n,2n)^{238}Pu cross section originating from modeling.

1 Introduction

The ^{239}Pu(n,2n)^{238}Pu cross section, between threshold and 15 MeV incident neutron energy, is uncertain although it plays an essential role in nuclear diagnostics. Direct neutron counting measurements below 14 MeV by Frehaut[1] and by Mather[2] differ significantly from each other both in magnitude and in the rise of the cross section near threshold. A third radio-chemical measurement by Lougheed exists near 14 MeV[3]. In order to obtain an improved understanding of the behavior of the ^{239}Pu(n,2n)^{238}Pu cross section both in terms of shape and magnitude, a

new approach was proposed at LLNL in 1995[4]. This method combines an experimental measurement of the ^{239}Pu(n,2nγ)^{238}Pu cross section for individual γ-rays with a theoretically calculated ratio of $^{239}\mathrm{Pu(n,2n}\gamma)/^{239}\mathrm{Pu(n,2n)}$ to infer the total ^{239}Pu(n,2n)^{238}Pu cross section. That is,

$$^{239}\mathrm{Pu(n,2n)}^{\mathrm{inferred}} = \frac{\{^{239}\mathrm{Pu(n,2n}\gamma)\}^{\mathrm{experiment}}}{\{^{239}\mathrm{Pu(n,2n}\gamma)/^{239}\mathrm{Pu(n,2n)}\}^{\mathrm{model}}} \,. \tag{1}$$

This report describes the LLNL calculations of the ratio,$^{239}\mathrm{Pu(n,2n}\gamma)/^{239}\mathrm{Pu(n,2n)}$, based on physics models and presents the inferred ^{239}Pu(n,2n)^{238}Pu cross section. The theoretical tool employed in our calculations is the IDA system of nuclear reaction codes[5]. All three classes of reaction mechanisms, namely, the direct, the preequilibrium, and the compound reactions are considered. In addition to particle emission, both fission and γ-cascade processes are included in the compound reaction. The calculations are performed for incident neutron energies ranging from 5.68 to 17.18 MeV. Inferred ^{239}Pu(n,2n)^{238}Pu cross sections from calculations using the reaction modeling code, GNASH[6], are also shown for comparison.

This report is organized as follows. First, the optical model potential that we use to calculate the elastic and direct inelastic scattering cross sections is described in Section 2, while the preequilibrium reaction is discussed in Section 3. In Section 4, compound processes which include particle emission, fission and γ-emission are discussed. The major parameters used in each physics model are tabulated. Section 5 presents results and discussions of the inferred ^{239}Pu(n,2n) cross sections followed by conclusions in Section 6.

2 The Optical Model Calculations

The direct reaction mechanism is described by the optical model, which describes the interaction between the projectile and the nucleons in the target nucleus by a nucleon-nucleus potential. Practical calculations employ one-body phenomenological potentials which consist of a real term, $V(r)$, which describes the scattering of the particle flux, and an imaginary term, $W(r)$, which accounts for the absorption of the particle flux by the target nucleus. In $V(r)$ and $W(r)$, r is the distance between the incoming particle and the target. The general form of the phenomenological potential is given by:

$$\begin{aligned} U(r) &= V(r) + iW(r) \qquad (2)\\ &= V(E_{\mathrm{inc}})f_V(r) && \text{real volume}\\ &\quad + iW_s(E_{\mathrm{inc}})g_W(r) && \text{imaginary surface}\\ &\quad + iW_V(E_{\mathrm{inc}})f_W(r) && \text{imaginary volume}\\ &\quad + d_{so}\vec{l}\cdot\vec{s}V_{so}h_{V_{so}}(r) && \text{real spin}-\text{orbit} \end{aligned}$$

$$+id_{so}\vec{l}\cdot\vec{s}W_{so}h_{W_{so}}(r) \qquad \text{imaginary spin}-\text{orbit}$$
$$+V_c(r) \qquad \text{Coulomb}$$

where $E_{\rm inc}$ is the energy of the projectile in the laboratory frame. Here, a Woods-Saxon potential is used for the volume potentials $f_V(r)$ and $f_W(r)$, that is,

$$f_j(r) = \frac{1}{1+\exp[(r-R_j)/a_j]} \qquad j = V, W \tag{3}$$

where $R_j = r_0 A^{1/3}$ is the radius of the nucleus and a_j is the diffuseness parameter. The surface potential is taken to be proportional to the derivative of the volume potential, i.e.,

$$g_W(r) = -4a_W \frac{d}{dr} f_W(r) = 4\frac{\exp\left[(r-R_W)/a_W\right]}{\left(1+\exp[(r-R_W)/a_W]\right)^2}\,. \tag{4}$$

For spin-orbit potentials, the Thomas form is used:

$$h_j(r) = -\frac{1}{r}\frac{d}{dr} f_j(r) = \frac{1}{r a_j}\frac{\exp\left[(r-R_j)/a_j\right]}{\left(1+\exp[(r-R_j)/a_j]\right)^2} \qquad j = V_{so}, W_{so}\,. \tag{5}$$

The spin-orbit constant $d_{so} = (\hbar/m_\pi c)^2$, where m_π is the pion mass. The strength of the various components of the optical model are embodied in the parameters V, W_S, W_V, V_{so}, and W_{so}, each of which is in principle a function of the incident energy $E_{\rm inc}$.

The phenomenological optical model potential is parametrized in terms of potential strengths and geometrical parameters[7, 8]. As usual, the geometrical parameters, R_j and a_j, are assumed to be energy independent. Since inelastic scattering and nuclear reactions preferentially occur at the surface of a nucleus at low incident energies, the absorptive potential is typically constructed to have only a surface component when $E_{\rm inc} \leq 10$ MeV, roughly. However, as $E_{\rm inc}$ increases, a volume imaginary potential is added to account for the interactions inside the nucleus. For the spin-orbit potentials, experimental evidence[8] suggests that W_{so} is very small for $E_{\rm inc} < 50$ MeV. Thus, in the energy range of 5.68 to 17.18 MeV and in the absence of Coulomb interactions, the coefficients $V(E_{\rm inc}), W_V(E_{\rm inc}), W_S(E_{\rm inc}), V_{so}$, as well as R and a ($a = a_j$) for each component, are the required parameters for the optical model potential.

Actinides are deformed. The effects of deformation in a target nucleus are accounted for within the coupled-channel formalism through the parametrization of the radius parameter R_j. That is, the volume and surface potentials are functions of $r - R_j(\{\alpha\})$ where the collective coordinates $\{\alpha\}$ describe the deformation of the target nucleus. Note that the spin-orbit component of the potential is taken to be non-deformed.

	$E_{\rm inc} \leq 10$ MeV	$E_{\rm inc} > 10$ MeV
real volume	$V_0 = 52$ MeV	
	$V_1 = -0.3$	
	$V_2 = 26$ MeV	same as $E_{\rm inc} \leq 10$ MeV
	$V_3 = -0.15$	
	$R = 1.25$ fm	
	$a = 0.63$ fm	
imaginary volume		$W_{V0} = -3.8$ MeV
		$W_{V1} = 0.38$
	0	$W_{V2} = -1.9$ MeV
		$W_{V3} = 0.19$
		$R = 1.27$ fm
		$a = 0.62$ fm
imaginary surface	$W_{S0} = 3.08$ MeV	$W_{S0} = 8.496$ MeV
	$W_{S1} = 0.4$	$W_{S1} = -0.1416$
	$W_{S2} = 1.54$ MeV	$W_{S2} = 4.248$ MeV
	$W_{S3} = 0.2$	$W_{S3} = -0.0708$
	$R = 1.27$ fm	$R = 1.27$ fm
	$a = 0.62$ fm	$a = 0.62$ fm
spin-orbit	$V_{so} = 6.2$ MeV	
	$R = 1.15$ fm	same as $E_{\rm inc} \leq 10$ MeV
	$a = 0.75$ fm	

Table 1: *Flap1.5 optical model potential parameters.*

The set of coupled-channel optical model parameters used in our calculations were derived by Dietrich and Ross for the actinides. The particular set employed is called Flap1.5 and is tabulated in Table 1. The energy dependence of the parameters $V(E_{\rm inc}), W_V(E_{\rm inc})$, and $W_S(E_{\rm inc})$ is as follows:

$$V(E_{\rm inc}) = V_0 + V_1 E_{\rm inc} - (V_2\epsilon + V_3\epsilon E_{\rm inc}) \quad (6)$$

$$W_V(E_{\rm inc}) = W_{V0} + W_{V1} E_{\rm inc} - (W_{V2}\epsilon + W_{V3}\epsilon E_{\rm inc}) \quad (7)$$

$$W_S(E_{\rm inc}) = W_{S0} + W_{S1} E_{\rm inc} - (W_{S2}\epsilon + W_{S3}\epsilon E_{\rm inc}) \quad (8)$$

where $\epsilon = (N - Z)/A$. In our calculations, the first 5 states of the ground-state band of ^{239}Pu are coupled. The excitation energy in keV, and the spin and parity, denoted by (E_x, J^π), of these 5 states are, respectively, $(0.0, \frac{1}{2}^+)$, $(7.861, \frac{3}{2}^+)$, $(57.276, \frac{5}{2}^+)$, $(75.706, \frac{7}{2}^+)$, $(163.76, \frac{9}{2}^+)$. The quadrupole and hexadecupole deformation parameters used for ^{239}Pu are $\beta_2 = 0.2$ and $\beta_4 = 0.06$.

Solutions of the Schrödinger equation using the given optical model potential yields the total cross section, $\sigma_{\rm t}$, the reaction cross section, $\sigma_{\rm R}$, the shape elastic

scattering cross section, $\sigma_{\rm se}$, as well as the direct inelastic scattering cross sections to the excited states that are coupled. The code used for the coupled-channel calculations is ECIS[9].

Figure 1 shows the calculated n + ^{239}Pu total cross section in comparison to the ENDL99[10] evaluation which has an estimated uncertainty of 1% above 300 keV of incident neutron energy. It is seen that the Flap1.5 potential reproduces the total cross section reasonably well.

The total cross section is related to the reaction cross section and the shape elastic cross section by

$$\sigma_{\rm t} = \sigma_{\rm se} + \sigma_{\rm R} \, . \tag{9}$$

In contrast to the excellent data that exist for the total cross section, the lack of data for the reaction cross section, or the shape elastic cross section, makes it difficult to arrive at a unique set of optical model parameters. For the same reason, it is difficult to quantify the error associated with the calculated $\sigma_{\rm R}$. In fact, different sets of optical model parameters that have been used for ^{239}Pu are known to generate reaction cross sections that differ from each other by 5% to 10%. Unfortunately, the magnitude of the reaction cross section is one of the major factors that control the magnitude of the calculated, relatively small, (n,2n) cross section, as well as cross sections of other reaction channels. The magnitude of the (n,2n) cross section is appreciable between the threshold, 5.647 MeV, and 17 MeV. Within this energy interval, the competing reaction channels are fission, (n,n') and (n,3n) (when $E_{\rm inc} \geq 12.65$ MeV). The capture and compound elastic scattering cross sections are very small in this energy range. We therefore have,

$$\sigma_{\rm R} \approx \sigma_{\rm f} + \sigma_{\rm n,n'} + \sigma_{\rm n,2n} + \sigma_{\rm n,3n} \, . \tag{10}$$

The reaction cross section, $\sigma_{\rm R}$, is of the order of barns. One easily sees that the uncertainty in $\sigma_{\rm R}$ will greatly affect the magnitude of $\sigma_{\rm n,2n}$, which peaks at a few hundred millibarns, even when the calculated fission cross section, which is a much stronger channel than the (n,2n), is fitted precisely to the experimental data available.

Fortunately, the inference of the (n,2n) cross section only depends on the calculated ratio of (n,2nγ)/(n,2n) as defined by Equation (1). Given both (n,2nγ) and (n,2n) are derived from $\sigma_{\rm R}$, the uncertainty in $\sigma_{\rm R}$ is partially removed in the ratio. The goal of the model calculations in the inference of the ^{239}Pu(n,2n) cross section is, therefore, to obtain as accurate a ratio of (n,2nγ)/(n,2n) as possible.

3 Preequilibrium Emission

Preequilibrium reactions take place on a time scale that is in between the direct and the compound processes. Because preequilibrium emissions occur before the

composite nucleus reaches its equilibrated state, the emitted particles, on average, bring with them more energy and orbital angular momentum than particles emitted via the compound reaction mechanism. In IDA, the preequilibrium reaction mechanism is described by a semi-classical exciton model[11] where the interaction between the incoming nucleon and the nucleus is approximated by a cascade of two-body interactions initiated by the projectile. For example, the projectile interacts with one of the nucleons in the target nucleus, lifting it from its prescribed single-particle orbital and creating a two-particle, one-hole, or equivalently, a three-exciton configuration. These three excitons can further interact, via two-body interactions, with the rest of the particles and holes in the system or with each other and create more complex configurations. Through this process, the energy of the projectile is spread among an increasing number of nucleons in the composite nucleus. The state of the nucleus at any given time is characterized by the number of excitons, n. The exciton model attempts to determine the probability, $q(n,t)$, that the composite system is comprised of n excitons at time t via the master equation

$$\frac{d}{dt}q(n,t) = \lambda^+(n-2)q(n-2,t)+\lambda^-(n+2)q(n+2,t)-q(n,t)\left[w(n)+\lambda^+(n)+\lambda^-(n)\right] . \tag{11}$$

In Equation (11), $\lambda^{\pm}(n) = \lambda_{n\to n\pm 2}$ are the average rates of internal transition from n-exciton states to those with $n \pm 2$, and

$$w(n) = \sum_b \int d\epsilon \; w_b(n,\epsilon) \tag{12}$$

where $w_b(n,\epsilon)$ is the average emission rate of particle type b with emission energy ϵ. Therefore, $w(n)$ is the total emission rate of all particles from state n of the composite nucleus. Based on the detailed balance principle, the solution of $w_b(n,\epsilon)$ can be obtained by considering the inverse process where a particle of type b with energy ϵ is absorbed to form the composite nucleus[12].

The transition rates are calculated from Fermi's Golden Rule via

$$\lambda_{n\to n'} = \frac{2\pi}{\hbar} M^2 \rho_{n'}(E^*) \tag{13}$$

where M^2 is the average of the square of the matrix element for two-body interactions between some initial and final states, and $\rho_{n'}(E^*)$ is the state density at the excitation energy E^* of the composite system for a given exciton number n'. In IDA calculations, Williams' approximation[13] to $\rho_{n'}(E^*)$ is used. The M^2 is parametrized according to Kalbach-Cline[14] as:

$$M^2 = k_{\rm pre} A^{-3} E^{*\,-1} \tag{14}$$

Once the solution of $q(n,t)$ is obtained, the differential cross section of emitting particle b, $d\sigma(a,b)/d\epsilon$, is computed by[11]

$$\frac{d\sigma}{d\epsilon}(a,b) = \sigma_a \sum_n w_b(n,\epsilon)\tau(n) \tag{15}$$

where

$$\tau(n) = \int_0^\infty q(n,t)dt \tag{16}$$

is the mean life-time for the exciton state n and σ_a is the cross section for formation of the composite nucleus from incident particle a and the target nucleus.

For the n + ^{239}Pu reaction between 5.68 and 17.18 MeV, particle emissions consist of almost only neutrons. In our calculations, the preequilibrium emission of the first outgoing neutron of the ^{239}Pu(n,2n)^{238}Pu reaction is considered. The magnitude of preequilibrium emission at various incident neutron energies is important because it affects the energy distribution of the excited states in the intermediate nucleus, ^{239}Pu, and consequently the residual nucleus, ^{238}Pu, in a different way than equilibrium emissions. It also affects the distribution of angular momentum of the populated states in the entry region of ^{238}Pu in a manner that is different from that arising from equilibrium neutron emissions, although this angular momentum effect associated with preequilibrium emission is not well-understood. Consequently, the magnitude of the preequilibrium emission plays an important role in determining the shape of the inferred ^{239}Pu(n,2n)^{238}Pu cross section. To obtain the value of $k_{\rm pre}$, which controls the strength of preequilibrium emission for a given $\rho_{n'}$, we compared the neutron emission spectrum at 14 MeV calculated from IDA, for the n + ^{239}Pu reaction, to that measured by Kammerdiener[15] for the n + ^{235}U reaction, as the two nuclei have similar properties. The emission spectra measured by Kammerdiener for the n + ^{239}Pu reaction are not used because of contamination present in the data. In extracting the emission spectrum of n + ^{235}U from data, fission neutrons are subtracted based on the evaluated fission spectrum and the $\bar{\nu}$ value from ENDF/B-VI[16]. Figure 2 shows that a value of $k_{\rm pre} = 300$ gives a good description of the data. However, there is a discrepancy between the calculation and experimental data at high emission energies, roughly $E_{\rm em} > 10$ MeV. This is believed to be due to the collective direct reaction mechanism that is not included in the preequilibrium model calculation. Thus, we adopt $k_{\rm pre} = 300$ in our calculations of preequilibrium emission.

Preequilibrium emission is more prevalent at higher incident neutron energies. Our calculation shows that at $E_{\rm inc} < 10$ MeV, the majority of the first generation of neutrons is emitted via the compound process. Beyond $E_{\rm inc} \approx 10$ MeV, the preequilibrium process quickly becomes dominant as can be seen in Figure 3. Also seen in the figure is that as $E_{\rm inc}$ increases, the direct component of the first-neutron emission, corresponding to excitation of the ground-state rotational band, steadily decreases, as does the compound component of the first neutron emission. This decrease in the direct component is simply a result of the diminishing effect of the coupling between channels.

4 Compound Processes

Once the cross sections for direct and the preequilibrium processes are calculated, they are subtracted from the reaction cross section, $\sigma_{\rm R}$. One then obtains the cross section of compound nucleus formation, $\sigma_a^{\rm CN}$, where a denotes the incident particle. The cross sections of various compound processes are subsequently calculated from the Hauser-Feshbach formulation[17], where the compound nucleus is treated as a thermally equilibrated system, and in which the formation and decay of such a compound nucleus are assumed to be independent of each other. The conservation of energy, angular momentum, and parity is enforced in the Hauser-Feshbach formalism as follows:

$$\begin{aligned} \epsilon + B_a &= \epsilon' + E' + B_{a'} = U & (17)\\ \vec{i} + \vec{I} + \vec{l} &= \vec{i'} + \vec{I'} + \vec{l'} = \vec{J} & (18)\\ p \cdot P \cdot (-1)^l &= p' \cdot P' \cdot (-1)^{l'} = \pi & (19) \end{aligned}$$

where the unprimed quantities are associated with the entrance channel with incident particle a, and the primed quantities represent the exit channel with outgoing particle a'. The center-of-mass kinetic energies are given by ϵ and ϵ', and B_a and $B_{a'}$ are the binding energies associated with particles a and a'. The excitation energy of the residual nucleus is denoted by E'. The spins and parities of the incoming and outgoing particles are labeled by $\vec{i}, p$ and $\vec{i'}, p'$, and those of the target and residual nuclei are given by $\vec{I}, P$ and $\vec{I'}, P'$. The orbital angular momenta are labeled by $\vec{l}, \vec{l'}$ and the total energy, spin, and parity of the compound nucleus are denoted by U, J, π. The notation used in this section closely follows that of Reference[12].

The Hauser-Feshbach expression for the mean angle-integrated cross section $\sigma_{a,a'}(\epsilon, I, P; \epsilon', I', P')$, for the reaction whose entrance channel is denoted by the $(a; \epsilon, I, P)$ and whose exit channel is represented by $(a'; \epsilon', I', P')$ is[18]:

$$\begin{aligned} \sigma_{a,a'}(\epsilon, I, P; \epsilon', I', P') &= \frac{\pi}{k_a^2} \sum_{J,\pi} \frac{2J+1}{(2i+1)(2I+1)} \{\sum_{lj} T_{alj}^J(\epsilon)\} \frac{\sum_{l'j'} T_{a'j'l'}^J(\epsilon')}{\sum_{a''l''j''\epsilon''} T_{a''l''j''}^J(\epsilon'')} \\ &= \sum_{J,\pi} \sigma_a^{\rm CN}(\epsilon, I, P; U, J, \pi) \frac{\sum_{l'j'} T_{a'j'l'}^J(\epsilon')}{\sum_{a''l''j''\epsilon''} T_{a''l''j''}^J(\epsilon'')} \qquad (20) \end{aligned}$$

where k_a is the wave number for the relative motion of the pair of particles in the entrance channel and $T_{alj}^J(\epsilon)$ is the transmission coefficient in this channel. The cross section of forming the compound nucleus with total energy U, angular momentum J and parity π from the entrance channel is denoted by $\sigma_a^{\rm CN}(\epsilon, I, P; U, J, \pi)$. The compound nucleus at a state (U, J, π) decays to a residual nucleus at a state (E', I', P'), by emitting particle a' with energy ϵ', and the transmission coefficient for the exit channel is $T_{a'j'l'}^J(\epsilon')$. The denominator of Equation (20) is a sum of

transmission coefficients over all possible decay channels from the compound nucleus in state (U, J, π). Depending on the energy, U, of the compound nucleus, the residual nucleus, after emitting the outgoing particle, can be left in an excited state that is either in the discrete region or in the continuum. Thus, the denominator generally consists of two components, that is:

$$\sum_{a''l''j''\epsilon''} T^J_{a''l''j''}(\epsilon'') = \sum_{a''l''j''}^{E^{a''}_{\rm cut}} T^J_{a''l''j''}(\epsilon'') + \sum_{a''l''j''I''} \int_{E^{a''}_{\rm cut}}^{E^{max,a''}} \omega_{a''I''}(E^{max,a''} - \epsilon'') T^J_{a''l''j''}(\epsilon'') d\epsilon'' \quad (21)$$

where $E^{a''}_{\rm cut}$ is where the discrete excitation energy region in the residual nucleus that corresponds to the ejectile a'' ends, and $\omega_{a''I''}(E^{max,a''} - \epsilon'')$ is the density of levels of spin I'' in the residual nucleus at energy $E^{max,a''} - \epsilon''$. The maximum kinetic energy in the center-of-mass system for the exiting channel with ejectile a'' is labeled by $E^{max,a''}$. Similarly, the numerator in the last factor of Equation (20) should be replaced by a product of transmission coefficient and level density if the exit channel $(a'; \epsilon', I', P')$ leaves the residual nucleus with an excitation energy that is in its continuum. In both Equations (20) and (21), angular momentum coupling rules must be satisfied.

In the range of incident neutron energies that is of interest to this work, three compound processes need to be considered. They are fission, neutron emission and γ-emission. As discussed in the previous sections, the compound nucleus formation cross section, $\sigma_a^{\rm CN}$, can be derived from calculations from the optical model and the exciton model. The Hauser-Feshbach calculation of the fission cross section, the neutron-emission cross section and the γ-emission cross section essentially translates into calculating the transmission coefficients for fission, neutron emission and γ-emission, denoted by T_f, T_n, and T_γ, respectively. The following subsections outline our calculations of each of these three processes.

4.1 Fission

Fission is a large component of the reaction cross section. Figure 4 shows that from 5.68 to 17.18 MeV, 50 % to over 70 % of the reaction cross section is attributed to fission. It is, therefore, important to calculate the fission cross section correctly since small variations in the fission cross section could significantly alter the calculated cross sections of weaker reaction channels such as ^{239}Pu(n,2n). Moreover, the accuracy of the energy dependence of the fission cross section affects the shapes of the ^{239}Pu(n,2n) and ^{239}Pu(n,2nγ) excitation functions. Most importantly, the treatment of fission may affect the calculated (n,2n)/(n,2nγ) ratio used to multiply the measured γ-yield to infer the total (n,2n) cross section. Fortunately, the fission cross section, ^{239}Pu(n,f), is well established experimentally. The determination of

the parameters used in calculating the fission cross section is therefore facilitated by requiring a good fit to the experimental data.

In calculating the fission cross section, $\sigma_{\rm f}$, we ignore details of the formation of fission products and the Hauser-Feshbach formula simplifies to:

$$\sigma_{\rm f}(\epsilon, I, P) = \sum_{J,\pi} \sigma_{\rm n}^{\rm CN}(\epsilon, I, P; U, J, \pi) \frac{T_{\rm f}(U, J, \pi)}{T(U, J, \pi)} \tag{22}$$

where $\sigma_{\rm n}^{\rm CN}(\epsilon, I, P; U, J, \pi)$ is the compound nucleus formation cross section from the $n + {}^{239}$Pu reaction, and $T_{\rm f}(U, J, \pi)$, $T(U, J, \pi)$ are fission and total transmission coefficients, respectively.

The experimental data only give total fission cross sections, which correspond to the left-hand-side of Equation (22). In order to treat fission as one of the competing channels in the compound process, the fission transmission coefficient, $T_{\rm f}(U, J, \pi)$, is needed and must be provided by a physical model. For our calculations, the double-humped fission barrier model of Bjørnholm and Lynn[19] is employed. In this model, the shapes of the two fission barriers are approximated by two parabolas. For a nucleus with excitation energy U, the penetration through a single barrier is given by Hill and Wheeler[20] as:

$$T(U, J, \pi) = \int_0^\infty \frac{\hat{\rho}(\zeta, J, \pi) d\zeta}{1 + \exp\left[\left(V(J) + \zeta - U\right)/\hbar\omega\right]} \tag{23}$$

where $V(J)$ is the fission barrier height at angular momentum J, and $\hbar\omega$ is the curvature of the barrier at the saddle point. An estimate of the quantitative decrease of the fission barrier height, ΔV, as angular momentum increases is given by Sierk[21] and the values are tabulated in Table 2. The level density for positive parity states is assumed to be the same as that for the negative parity states. That is, $\hat{\rho}(\zeta, J, \pi = +1) = \hat{\rho}(\zeta, J, \pi = -1) = (1/2)\tilde{\rho}(\zeta, J)$. The functional dependence of $\tilde{\rho}(\zeta, J)$ on J is given by:

$$\tilde{\rho}(\zeta, J) = \rho_J(J)\rho(\zeta) = \frac{(2J+1)\exp\left[-\left(J+1/2\right)^2/2\sigma^2\right]}{2\sqrt{2\pi}\sigma^3}\rho(\zeta)\,, \tag{24}$$

where σ^2 is the spin cut-off parameter and the dependence of the density of states, $\rho(\zeta)$, on the excitation energy ζ, which is measured from the top of the barrier, is assumed to be of the constant temperature type:

$$\rho(\zeta) = \sum_J \tilde{\rho}(\zeta, J) = C\exp\left[\zeta/\theta\right] \tag{25}$$

for low excitation energies where θ is the nuclear temperature and C is a constant. For higher excitation energies, a Fermi-gas behavior is adopted:

$$\rho(\zeta) = D\frac{\exp(2\sqrt{aE^*})}{a^{1/4}E^{*5/4}}\frac{\sqrt{\pi}}{12} \tag{26}$$

J	0	1	2	3	4	5	6	7
ΔV (MeV)	0	0.002	0.004	0.008	0.012	0.017	0.022	0.029
J	8	9	10	11	12	13	14	15
ΔV (MeV)	0.036	0.044	0.052	0.061	0.070	0.081	0.092	0.104
J	16	17	18	19	20	21	22	23
ΔV (MeV)	0.116	0.129	0.143	0.157	0.172	0.188	0.204	0.221
J	24	25	26	27	28	29	30	31
ΔV (MeV)	0.238	0.256	0.274	0.293	0.313	0.333	0.354	0.375
J	32	33	34	35	36			
ΔV (MeV)	0.397	0.419	0.442	0.465	0.489			

Table 2: *Decrease of fission barrier V at given angular momentum J. For $J > 36$, a linear extrapolation of $\Delta V(J) = 0.489 + (J - 36) \times 0.024$ is used.*

where

$$E^* = \zeta - P(Z) - P(N) \tag{27}$$

and $P(Z)$, $P(N)$ are the proton and neutron pairing energies suggested by Gilbert and Cameron[22]. The level density parameter a is treated as an adjustable parameter and D is a constant. A further assumption that the two fission barriers, labeled by A and B, are uncorrelated is made. The resulting fission transmission coefficient through both barriers is simply:

$$T_{\rm f}(U, J, \pi) = \frac{T_A(U, J, \pi) T_B(U, J, \pi)}{T_A(U, J, \pi) + T_B(U, J, \pi)} \,. \tag{28}$$

Following Bjørnholm and Lynn, the excitation energy ζ is divided into several ranges. The first few of these segments employ the constant-temperature level density while the last one uses the Fermi-gas level density. Constants C, θ, a, and to some extent σ^2, are treated as free parameters in order to reproduce the experimental fission cross section. The continuity of level density $\rho(\zeta)$ is imposed throughout all segments of the excitation energy. As a result, apart from the constant C in the first segment, all other values of C as well as D in Equation (26) are automatically determined by the continuity constraint. We also ensure the continuity of the spin cut-off parameter, σ^2. In the constant-temperature regions, the spin cut-off parameter is linearly interpolated from its initial value at the lower bound of the excitation energy segment to the initial value of σ^2 at the beginning of the next energy segment. The σ^2 in the Fermi-gas region has an energy dependence of

$$\sigma^2(E^*) = 0.0888 A^{2/3} \sqrt{a E^*} \tag{29}$$

where E^* is defined in Equation (27). The fission barrier heights at $J = 0$ and the curvatures for the involved nuclei are tabulated in Table 3 while the level density

	V_A (MeV)	$\hbar\omega_A$ (MeV)	V_B (MeV)	$\hbar\omega_B$ (MeV)
^{240}Pu	5.57	1.05	4.90	0.60
^{239}Pu	6.25	0.70	5.70	0.52
^{238}Pu	6.00	1.04	5.40	0.60

Table 3: *Fission barrier heights at $J = 0$ and fission barrier curvatures at the saddle points for barriers A and B for the three nuclei that fission in the incident-neutron-energy range of* 5.68 *to* 17.18 *MeV.*

parameters for various excitation ranges and both barriers A and B are listed in Table 4.

As can be seen from Figure 4, the adjusted parameters give rise to a calculated fission cross section that reproduces the evaluations well. Quantitatively, the calculated fission cross section differs from that evaluated by less than the uncertainty of the evaluations which is about 2 %. The two sets of evaluations, ENDL99 and JENDL3.3[23], are both entirely based on experimental measurements. They agree with each other well except in the region near 14 MeV of incident neutron energy where the difference between the two evaluations is about 5 %.

4.2 Neutron Emission

The calculation of neutron-emission cross sections follows the Hauser-Feshbach formulation given by Equation (20). For particle emission, the transmission coefficients are provided by the optical model calculations[7, 8].

The Hauser-Feshbach calculation of neutron emission, as well as other reaction channels, critically depends on the level densities employed. In our calculations, the Gilbert-Cameron level density prescription[22] is employed for the neutron emission channel. In this level density formulation, a constant-temperature form is used at excitation energy $U^* \leq U_x^*$ and a Fermi-gas form is used for $U^* > U_x^*$. In complete analogy to Equation (27), we have, $U^* = U - P(Z) - P(N)$ where U is the excitation energy of a given nucleus. The difference between ζ, in Equation (27), and U is that ζ is measured from the top of a fission barrier when a nucleus is deformed to its pre-scission state whereas U is measured from the ground state of a nucleus with normal deformation.

The various level density parameters used in the particle emission channels in our calculations are listed in Table 5. Parameter $E_{\rm cut}$ is the maximum excitation energy of the discrete states beyond which the continuous level density is modeled by the Gilbert-Cameron formulation. With the exception of ^{238}Pu, the determination of $E_{\rm cut}$ for each nucleus is based on the available discrete level scheme from ENSDF[24]. The spin cut-off parameters σ^2, at excitation energy $E_{\rm cut}$, are derived from the analysis of spin distribution of the discrete levels in each nucleus and

	ζ	ld	$\sigma_{\rm init}$	C_A	θ_A	C_B	θ_B	a_A	a_B
	MeV		MeV		MeV		MeV	MeV^{-1}	MeV^{-1}
^{240}Pu	$0.0 \rightarrow 1.5$	CT	5.1	1.35	0.2652	1.65	0.3153		
	$1.5 \rightarrow 3.0$	CT	5.7		0.3690		0.3740		
	$3.0 \rightarrow 6.0$	CT	6.3		0.4000		0.4020		
	> 6.0	FG	formula					32	32
^{239}Pu	$0.0 \rightarrow 1.2$	CT	5.7	650.0	0.4100	550.0	0.4150		
	$1.2 \rightarrow 7.0$	CT	6.4		0.5050		0.5150		
	> 7.0	FG	formula					31	31
^{240}Pu	$0.0 \rightarrow 0.6$	CT	5.6	9.0	0.3700	7.0	0.3800		
	$0.6 \rightarrow 3.2$	CT	5.7		0.3800		0.3900		
	$3.2 \rightarrow 7.0$	CT	6.5		0.6500		0.6590		
	> 7.0	FG	formula					30	30

Table 4: *Parameters used in level density formulae above the two fission barriers labeled by A and B. The spin cut-off parameter $\sigma_{\rm init}$ is the initial value of σ at the beginning of a given energy segment. The third column indicates if the level density used in the corresponding energy interval is constant temperature (CT) or Fermi gas (FG). The $\sigma_{\rm init}$ for the Fermi-gas segment is determined by the formula given in Equation (29). The constant D in Equation (26) is not tabulated in the table since it is determined according to the continuity constraint. For the same reason, the constant C in Equation (25) for those energy segments other than the very first is not shown in the table.*

	$E_{\rm cut}$ (MeV)	σ^2 (MeV^2)	U_x^* (MeV)	a (MeV^{-1})
^{240}Pu	1.162	10.3	3.16	27.01
^{239}Pu	0.5375	46.2	3.48	27.48
^{238}Pu	1.33	29.8	3.55	26.25
^{237}Pu	0.3	7.98	3.81	27.14

Table 5: *Level density parameters for ^{240}Pu, ^{239}Pu, ^{238}Pu, and ^{237}Pu.*

are shown in Table 5. Again, this analysis is based on the available experimental information from ENSDF. A linear interpolation of σ^2 between the values listed in Table 5 and the initial value of the spin cut-off parameter at the beginning of the Fermi-gas segment is carried out. The energy dependence of the spin cut-off parameter for the Fermi-gas level density is in the same form as that used in the fission channel (cf. Equation (29)). That is, $\sigma^2 = 0.0888A^{2/3}\sqrt{aU^*}$. The Fermi-gas level-density parameter, a, is determined by the statistical analyses of neutron resonance data at the neutron binding energy. With a given level density at the

neutron binding energy and with the knowledge of the number of levels below $E_{\rm cut}$, values of a and U_x^* can be obtained by requiring that the level density and its derivative be continuous at U_x^*.

Using the parameters in Table 5, it is instructive to see the model prediction of the compound component of the neutron-emission cross section versus the preequilibrium component for the (n,2n) reaction channel. The outcome reflects the interplay between the modeling of the preequilibrium mechanism and the modeling of the compound mechanism, as well as the competition between various compound reaction channels, such as fission, (n,n'), (n,3n), and γ-emission. Figure 5 shows the IDA calculations of the fractions of the compound and preequilibrium components of the (n,2n) cross section relative to the total (n,2n) cross section. It should be pointed out that only the first neutron emission has a preequilibrium component. It is seen from the figure that the preequilibrium component is a very small fraction of the (n,2n) cross section at low $E_{\rm inc}$, as expected. However, it becomes comparable to the compound component near $E_{\rm inc} = 12$ MeV and quickly becomes dominant afterwards. As mentioned in Section 3, the relative strength of the preequilibrium emission to the compound emission has an effect on the shape of the (n,2n) excitation function. Moreover, because the spin distribution in the residual nucleus, ^{238}Pu, following a preequilibrium neutron emission from the composite nucleus, ^{240}Pu, is different from that following a compound neutron emission, their relative strength , although not the only factor, would impact the relative populations of states with different spin, J, in the residual nucleus. Comparisons between the calculated relative populations of some states in the residual nucleus ^{238}Pu and GEANIE measurements are discussed in the next subsection.

4.3 γ Emission

In our calculations, γ-emission is considered as a compound process. What is required in order to calculate the cross section of γ-emission is therefore the γ-transmission coefficients. Similar to fission, the γ-transmission coefficients are obtained from a separate physical model that approximates the γ-emission mechanism. In particular, the detailed balance principle is applied to relate the averaged partial radiative width of γ-emission, $\langle\Gamma_\gamma^{\rm XL}(f \to i)\rangle$, from state f to state i of a nucleus, to the cross section of the inverse photon absorption process. Here, the state f is characterized by (E_f, J_f, π_f) and the state i is labeled with quantum numbers (E_i, J_i, π_i). The detailed-balance principle leads to[25, 26]:

$$\langle\sigma_\gamma^{\rm XL}(i \to f)\rangle = \pi^2 \lambda\!\!\!^{-2} g_{if} \langle\Gamma_\gamma^{\rm XL}(f \to i)\rangle / D_f \tag{30}$$

where $\langle\sigma_\gamma^{\rm XL}(i \to f)\rangle$ is the averaged cross section for the absorption of one photon of energy $\epsilon_\gamma = E_f - E_i$ and multipole type XL from the state i of a nucleus to the state f. The photon wavelength is given by $\lambda\!\!\!^{-} = \hbar c/\epsilon_\gamma$ and $g_{if} = (2J_f+1)/(2J_i+1)$ is a statistical factor. D_f is the mean spacing of resonances with spin J_f, parity π_f,

and energy E_f. With the usual definition[27], the γ-ray strength function, $f^{\mathrm{XL,J_f\pi_f}}_{\gamma,J_i\pi_i}$, can be expressed in terms of the averaged radiative width of γ-emission as follows:

$$f^{\mathrm{XL,J_f\pi_f}}_{\gamma,J_i\pi_i} = \frac{\langle \Gamma^{\mathrm{XL}}_{\gamma}(f \rightarrow i) \rangle}{\epsilon^{2L+1}_{\gamma} D_f} \,. \tag{31}$$

The strength functions are assumed to be independent of spin and parity. That is,

$$f^{\mathrm{XL,J_f\pi_f}}_{\gamma,J_i\pi_i}(\epsilon_\gamma) = f^{\mathrm{XL}}_{\gamma}(\epsilon_\gamma) \,, \tag{32}$$

and the transmission coefficients for γ-emission, $T^{\mathrm{XL}}_{\gamma}(\epsilon_\gamma)$, are defined in terms of the γ-ray strength functions. The transmission coefficients, $T^{\mathrm{XL}}_{\gamma}(\epsilon_\gamma)$, are, therefore, related to the photon absorption cross section by:

$$T^{\mathrm{XL}}_{\gamma}(\epsilon_\gamma) = 2\pi\epsilon^{2L+1}_{\gamma} f^{\mathrm{XL}}_{\gamma}(\epsilon_\gamma) = \frac{2\epsilon^2_{\gamma}\langle \sigma^{\mathrm{XL}}_{\gamma}(i \rightarrow f) \rangle}{\pi\hbar^2 c^2 g_{if}} \,. \tag{33}$$

When evaluating the photon absorption cross section, we use the Brink-Axel[28, 29] hypothesis which allows the absorption cross section of a photon by a nucleus at an excited state to be equated to that by the nucleus at its ground state:

$$\langle \sigma^{\mathrm{XL}}_{\gamma}(i \rightarrow f) \rangle = \frac{2J_f + 1}{3(2J_i + 1)} \sigma_{\mathrm{gs}}(\epsilon_\gamma) \tag{34}$$

where $\sigma_{\mathrm{gs}}(\epsilon_\gamma)$ is the cross section of absorbing a photon with energy ϵ_γ by a nucleus at its ground state and its dependence on ϵ_γ is approximated by one or two Lorentzians, namely,

$$\sigma_{\mathrm{gs}}(\epsilon_\gamma) = \sum_{q=1,2} \sigma_q \frac{\epsilon^2_{\gamma}\Gamma^2_q}{(\epsilon^2_{\gamma} + E^2_q)^2 + \epsilon^2_{\gamma}\Gamma^2_q} \,. \tag{35}$$

The constants σ_q, Γ_q, and E_q are the peak cross section, peak energy, and width at half maximum of the Lorentzian, respectively. Their values are derived from systematics and are known to provide photon absorption cross sections due to the $E1$ giant dipole resonance to within a few percent in some tested cases[25]. In IDA calculations, γ-emission of the multipole types $E1$,$M1$, and $E2$ are considered. For the dominant $E1$ radiation, the splitting of the giant resonance in deformed Pu isotopes is taken into account by a superposition of two Lorentzians. Table 6 lists the values of σ_q, Γ_q, and E_q parameters used in IDA calculations.

The modeling of the γ-cascade is very important because it affects the ratios of ^{239}Pu(n,2nγ)/^{239}Pu(n,2n), which in turn affect the total ^{239}Pu(n,2n) cross section inferred from Equation (1). Apart from the γ-ray transmission coefficients, the initial and final level densities associated with the γ-transition also play a critical role in the competition between γ-decay and other reaction channels. Furthermore, the

	^{240}Pu	^{239}Pu	^{238}Pu	^{237}Pu
σ_1^{E1} (barn)	0.301	0.300	0.297	0.296
Γ_1^{E1} (MeV)	2.68	2.68	2.69	2.70
E_1^{E1} (MeV)	11.55	11.56	11.62	11.63
σ_2^{E1} (barn)	0.408	0.406	0.404	0.402
Γ_2^{E1} (MeV)	3.80	3.80	3.80	3.81
E_2^{E1} (MeV)	13.82	13.83	13.84	13.85
σ^{M1} (barn)	0.043	0.043	0.043	0.043
Γ^{M1} (MeV)	1.48	1.48	1.48	1.49
E^{M1} (MeV)	7.40	7.41	7.42	7.43
σ^{E2} (barn)	0.043	0.042	0.042	0.042
Γ^{E2} (MeV)	1.52	1.52	1.52	1.53
E^{E2} (MeV)	10.14	10.15	10.17	10.18

Table 6: *Parameters used in the Lorentzian form of the photon absorption cross section. The peak cross section, peak energy, and half maximum width of the photon absorption cross section as a function of the photon energy, ϵ_γ, are denoted by σ, E, and Γ, respectively. The multipole type XL=$E1$,$M1$,$E2$ of photon absorption are indicated by superscripts. The splitting of the $E1$ giant dipole resonance is represented by a superposition of two Lorentzians subscripted by 1 and 2, respectively.*

angular momentum and parity selection rules imposed on the γ-transitions of multipole type XL, make the prediction of γ-cascade sensitive to the detailed structure, such as the spin and parity distribution, of the nucleus in question. In particular, the level scheme employed in the low excitation energy region, where a statistical treatment of the level density is not justified and where the collective nature of nuclear excitation is most pronounced, has direct impact on the population of a given low-lying excited state. One therefore would like to have as complete a level scheme as possible in order to account for the structure effects in the discrete region. Unfortunately, the experimental data in the ENSDF library are limited.

For the calculation of the ^{239}Pu(n,2nγ)/^{239}Pu(n,2n) ratios, the level scheme of the residual nucleus, ^{238}Pu, is most important. One finds, in the ENSDF data base, that the experimental measurements of bands such as the octupole and β-bands only extend to less than 1 MeV of excitation energy for this nucleus. Since the GEANIE measurements provide, with branching ratios known from other experiments, the cross sections of the population of a few discrete states in ^{238}Pu of excitation energy up to 1.083 MeV, it is essential to extrapolate the bands to beyond 1.083 MeV in order to reasonably simulate the physical γ-cascade in the discrete region and compare with GEANIE data. We therefore extended 8 of the 9 existing bands in ^{238}Pu. All bands are assumed to be rotational in nature and the

	index	π	E_x	J	branching ratios
^{240}Pu	1	+	0.0	0	
	2	+	0.043	2	1(100%)
	3	+	0.142	4	2(100%)
	4	+	0.294	6	3(100%)
	5	+	0.498	8	4(100%)
	6	-	0.597	1	1(38%),2(62%)
	7	-	0.649	3	2(49%),3(51%)
	8	-	0.742	5	3(13%),4(87%)
	9	+	0.748	10	5(100%)
	10	+	0.861	0	2(53%),6(47%)
	11	+	0.900	2	1(5%),2(13%),3(32%),6(27%),7(23%)
	12	-	0.938	1	1(89%),2(5%),6(5%),7(1%)
	13	-	0.959	2	2(92%),6(4%),7(4%)
	14	+	0.992	4	4(34%),7(47%),8(19%)
	15	-	1.002	3	2(100%)
	16	+	1.031	3	2(75%),3(25%)
	17	-	1.038	4	3(91%),7(6%),8(3%)
	18	+	1.042	12	9(100%)
	19	+	1.076	4	2(29%),3(71%)
	20	+	1.089	0	2(100%)
	21	-	1.116	5	3(90%),4(5%),7(5%)
	22	+	1.132	2	1(35%),2(18%),3(47%)
	23	+	1.137	2	1(40%),2(60%)

Table 7: *Discrete spectroscopy of ^{240}Pu. Excitation energy, E_x, is in units of MeV.*

determination of the branching ratios from an added state to others is based on the assumption that the transition matrix elements for a given multipole type to various states are the same. Consequently, for a given multipole type, the branching ratios depend only on the γ-ray energy of the transition. Tables 7 to 9 tabulate the discrete spectroscopy for the Pu isotopes used in our calculations. Only for ^{238}Pu did we extend the level scheme; the discrete levels used for the rest of the isotopes are strictly from ENSDF. The added levels in ^{238}Pu and their associated branching ratios estimated by us are indicated by an asterisk in column 4 of Table 9. If a level exists in ENSDF without branching ratios, we also give our estimates and these cases are indicated by an asterisk in the last column where branching ratios are given.

As an examination of the effect of discrete spectroscopy, we compared our calculations of the relative γ-ray intensities of $(8^+ \rightarrow 6^+)/(6^+ \rightarrow 4^+)$ and $(5^- \rightarrow 6^+)/(6^+ \rightarrow 4^+)$ in the ^{238}Pu nucleus, to that obtained from the GEANIE exper-

	index	π	E_x	J	branching ratios
^{239}Pu	1	+	0.0	1/2	
	2	+	0.008	3/2	1(100%)
	3	+	0.057	5/2	1(54%),2(46%)
	4	+	0.076	7/2	2(83%),3(17%)
	5	+	0.164	9/2	3(89%),4(11%)
	6	+	0.193	11/2	4(100%)
	7	+	0.285	5/2	1(2%),2(48%),3(38%),4(12%)
	8	+	0.318	13/2	5(100%)
	9	+	0.330	7/2	2(2%),3(23%),4(32%),5(5%),7(38%)
	10	+	0.358	15/2	6(100%)
	11	+	0.387	9/2	4(22%),7(11%),9(67%)
	12	-	0.392	7/2	3(7%),4(5%),7(84%),9(4%)
	13	-	0.434	9/2	12(100%)
	14	+	0.462	11/2	4(70%),5(19%),6(11%)
	15	-	0.470	1/2	1(37%),2(63%)
	16	-	0.487	11/2	12(95%),13(5%)
	17	-	0.492	3/2	1(35%),2(6%),3(59%)
	18	-	0.506	5/2	2(45%),3(4%),4(51%)
	19	+	0.512	7/2	7(75%),9(23%),11(2%)
	20	+	0.519	17/2	8(100%)
^{237}Pu	1	-	0.0	7/2	
	2	-	0.048	9/2	1(100%)
	3	-	0.106	11/2	1(95%),2(5%)
	4	+	0.146	1/2	1(100%)
	5	+	0.155	3/2	4(100%)
	6	-	0.175	13/2	2(95%),3(5%)
	7	+	0.201	5/2	4(68%),5(32%)
	8	+	0.224	7/2	5(100%)
	9	-	0.257	15/2	3(95%),6(5%)
	10	+	0.280	5/2	1(99%),5(1%)

Table 8: *Discrete spectroscopy of ^{239}Pu and ^{237}Pu. Excitation energy, E_x, is in units of MeV.*

iments corrected for internal conversion. Figures 6 and 7 show the results. The calculations are carried out with two different level schemes of ^{238}Pu. One has 20 levels which are provided strictly by ENSDF. In this case, $E_{\rm cut} = 1.173$ MeV. The other is the extended level scheme with 39 levels and $E_{\rm cut} = 1.33$ MeV. Clearly seen from the figures is that the extended level scheme gives rise to a greatly improved agreement with experimental data, and therefore a more realistic simulation of the

	index	π	E_x	J	branching ratios
^{238}Pu	1	+	0.0	0	
	2	+	0.044	2	1(100%)
	3	+	0.146	4	2(100%)
	4	+	0.303	6	3(100%)
	5	+	0.513	8	4(100%)
	6	-	0.605	1	1(42%),2(58%)
	7	-	0.661	3	2(60%),3(40%)
	8	-	0.763	5	3(43%),4(55%),7(2%)*
	9	+	0.774	10	5(100%)
	10	-	0.911*	7	4(92%),5(5%),8(3%)
	11	+	0.942	0	1(36%),2(62%),6(2%)
	12	-	0.963	1	1(52%),2(43%),6(4%),7(1%)
	13	-	0.968	2	2(100%)
	14	+	0.983	2	1(56%),2(20%),3(21%),6(2%),7(1%)
	15	-	0.985	2	2(95%),6(2%),7(3%)
	16	-	1.025*	3	2(53%),3(47%)
	17	+	1.028	2	1(41%),2(57%),3(2%)
	18	+	1.070	3	2(77%),3(23%)
	19	+	1.080	12	9(100%)
	20	+	1.081*	4	2(30%),3(40%),4(22%),7(5%),8(3%)
	21	-	1.083	4	3(91%),7(5%),8(2%),13(2%)
	22	-	1.085*	4	3(100%)
	23	-	1.103*	9	5(80%),9(5%),10(15%)
	24	+	1.126	4	2(13%),3(37%),4(5%),18(45%)*
	25	-	1.139*	5	21(100%)
	26	-	1.172*	5	3(45%),4(43%),7(5%),8(3%),22(4%)
	27	+	1.174	2	1(45%),2(55%)
	28	+	1.192*	5	3(30%),4(20%),24(50%)
	29	-	1.203	3	17(20%),18(2%),21(78%)
	30	-	1.211*	6	25(100%)
	31	+	1.229	0	1(8%),2(92%)
	32	+	1.231*	6	3(18%),4(45%),8(18%),10(16%),20(3%)
	33	-	1.257*	4	18(20%),25(80%)
	34	+	1.264	2	2(70%),3(30%)*
	35	+	1.268*	6	3(10%),4(30%),28(60%)
	36	-	1.294*	6	4(50%),8(25%),10(20%),26(5%)
	37	-	1.295*	7	30(100%)
	38	+	1.310	2	2(100%)
	39	-	1.321*	5	24(20%),30(80%)

Table 9: *Discrete spectroscopy of ^{238}Pu. Excitation energy, E_x is in units of MeV. The asterisks in column 4 indicate the levels we generate along with our estimates of their branching ratios. The asterisks in the last column label the levels that are in the ENSDF database without branching ratios, and for which we provide our estimates.*

γ-cascade. Also apparent is the difference in the predicted relative γ-ray intensities solely due to discrete spectroscopy. For example, the γ-ray intensity ratio of $(8^+ \rightarrow 6^+)/(6^+ \rightarrow 4^+)$, where the 8^+, 6^+, and 4^+ states are all members of the ground-state band, differs by about 20 % when using the two different level schemes of ^{238}Pu. This reveals the sensitivity of the γ-cascade calculations to the discrete spectroscopy included as model input. Of course, the discrete spectroscopy is not the only factor that influences the γ-cascade process. The initial distribution in energy and spin of the populated states in ^{238}Pu before the γ-cascade takes place certainly affects the relative strengths of the population of various low-lying states reached by the deexcitation of γ's. As discussed in Section 4.2, such initial distribution is a result of the interplay between the relative strengths of preequilibrium neutron emission, fission, compound emission of neutrons and γ's, as well as the angular momentum transfer mechanisms associated with each process. The calculations shown in Figures 6 and 7 have the same initial distribution of energy and angular momentum in ^{238}Pu, and therefore the differences reflect the different ^{238}Pu level scheme only.

Finally, we point out that the branching ratios from the 5^- state at 0.763 MeV in the octupole band, among some other levels, are unknown. In the level scheme of ^{238}Pu with 20 levels, this state is assumed to decay to the 3^- state of the same band with a branching ratio of 100 %. In the extended level scheme, we allowed inter-band transitions and adjusted the branching ratios from the 5^- state so that they agree with the measured relative γ-ray intensity of $(5^- \rightarrow 6^+)/(6^+ \rightarrow 4^+)$. The detailed branching ratios are given in Table 9. Figures 6 and 7 show that the transition rates from this state greatly affect the relative population of the discrete states in its vicinity. Their precise measurements are therefore desirable. We also note that no adjustments of branching ratios are made for states of the ground-state band as well as most of the states provided by ENSDF. Consequently, the two different calculations shown in Figure 6 are, to a large extent, a reflection of the extension of the level scheme, although the adjustment of the branching ratios of the 5^- state does affect the relative γ-ray intensity of $(8^+ \rightarrow 6^+)/(6^+ \rightarrow 4^+)$. The good agreement with data seen in both Figure 6 and Figure 7 suggests that our overall estimate of the branching ratios from the added levels and from the levels for which experimental branching ratios are absent in ENSDF, is reasonable.

5 Results and Discussions

The previous sections give a description of the major components of physics that are adopted in modeling various nuclear reaction cross sections. We now present the calculated ratios, ^{239}Pu(n, 2nγ)/^{239}Pu(n, 2n), and the final inferred ^{239}Pu(n,2n) cross sections.

number	initial level		final level		ϵ_γ (MeV)
	J^π	E_x (MeV)	J^π	E_x (MeV)	
1	6^+	0.303	4^+	0.146	0.157*
2	8^+	0.513	6^+	0.303	0.210
3	5^-	0.763	6^+	0.303	0.460
4	$3^-/5^-$	0.661/0.763	$2^+/4^+$	0.044/0.146	0.460*
5	1^-	0.963	2^+	0.044	0.919*
6	2^-	0.968	2^+	0.044	0.924*
7	4^-	1.083	4^+	0.146	0.937*

Table 10: *The seven γ-transitions in ^{238}Pu observed by GEANIE. The asterisks in the last column indicate transitions that decay to the ground state of ^{238}Pu via independent paths.*

5.1 Consistency of Inferred ^{239}Pu(n,2n) Cross Sections

The experimental input to the inferred ^{239}Pu(n,2n) cross section comes from the measured partial ^{239}Pu(n,2nγ)^{238}Pu cross sections. Seven γ-transitions following the two-neutron emission from the n + ^{239}Pu reaction are observed by GEANIE and they are listed in Table 10.

To examine the accuracy of the modeling, one meaningful direct comparison between theoretical calculations and the experimental GEANIE data is the relative γ-ray intensities for transitions between discrete states in ^{238}Pu, as discussed at the end of Section 4.3. Our attention is focused on comparing the model calculation of the relative γ-ray intensities for the lower-lying states to the corresponding γ-ray intensities derived from GEANIE data. The reason for focusing on lower-lying states is three-fold. First of all, the lower-lying states are fed more strongly and, hence, the modeling of the population of these states carries less uncertainty than that of states that are weakly populated where the magnitude of the cross section is rather small. Secondly, the band heads of high-K bands tend to lie at higher excitation energies than that of the low-K bands. The absence of conservation of the K quantum number in the γ-cascade model presently used suggests that the theoretical calculation of the population of the high-K states may be a less accurate representation of physical reality than the calculation of lower-lying states. Thirdly, the higher the excited state, the closer it is to $E_{\rm cut}$ where the discrete spectroscopy is replaced by a continuous statistical level density formulation. This results in greater loss of the structure effects in the modeling of the population of the state. Consequently, we compare the relative γ-ray intensity of $(8^+ \rightarrow 6^+)/(6^+ \rightarrow 4^+)$ where all the states belong to the ground-state band, and the relative γ-ray intensity of $(5^- \rightarrow 6^+)/(6^+ \rightarrow 4^+)$ where the 5^- state at 0.763 MeV is a state from the octupole band. The fact that both our calculated relative γ-ray

intensities, $(8^+ \rightarrow 6^+)/(6^+ \rightarrow 4^+)$ and $(5^- \rightarrow 6^+)/(6^+ \rightarrow 4^+)$, agree with GEANIE data, within experimental errors, implies that if one is to infer the ^{239}Pu(n,2n) cross section from the ratios $(6^+ \rightarrow 4^+)/(n,2n)$, $(8^+ \rightarrow 6^+)/(n,2n)$, and $(5^- \rightarrow 6^+)/(n,2n)$, separately, one should obtain consistent inferred ^{239}Pu(n,2n) cross sections within the experimental uncertainty. In other words, if we define

$$^{239}Pu(n,2n)_1^{\rm inferred} = \frac{\left\{^{239}{\rm Pu(n,2n}\gamma^{6^+\rightarrow 4^+})\right\}^{\rm experiment}}{\left\{^{239}{\rm Pu(n,2n}\gamma^{6^+\rightarrow 4^+})/^{239}{\rm Pu(n,2n)}\right\}^{\rm model}} \quad (36)$$

$$^{239}Pu(n,2n)_2^{\rm inferred} = \frac{\left\{^{239}{\rm Pu(n,2n}\gamma^{8^+\rightarrow 6^+})\right\}^{\rm experiment}}{\left\{^{239}{\rm Pu(n,2n}\gamma^{8^+\rightarrow 6^+})/^{239}{\rm Pu(n,2n)}\right\}^{\rm model}} \quad (37)$$

$$^{239}Pu(n,2n)_3^{\rm inferred} = \frac{\left\{^{239}{\rm Pu(n,2n}\gamma^{5^-\rightarrow 6^+})\right\}^{\rm experiment}}{\left\{^{239}{\rm Pu(n,2n}\gamma^{5^-\rightarrow 6^+})/^{239}{\rm Pu(n,2n)}\right\}^{\rm model}}\,, \quad (38)$$

we would have

$$^{239}Pu(n,2n)_1^{\rm inferred} \approx^{239} Pu(n,2n)_2^{\rm inferred} \approx^{239} Pu(n,2n)_3^{\rm inferred} \quad (39)$$

when experimental uncertainties are considered. Figure 8 shows that this is indeed the case. One sees from the figure that the fluctuation of the points near threshold is large. This is mostly due to the fact that both the measured partial cross sections and the calculated ratios in this region are small. Hence, slight changes in the magnitude of either would lead to a large variation in the inferred (n,2n) cross section. In addition, fluctuations from GEANIE data also contribute to the unsmooth behavior of the inferred ^{239}Pu(n,2n) cross sections. For example, at 8.11 MeV (c.f. Figure 9), the low GEANIE value of the $8^+ \rightarrow 6^+$ partial cross section causes the inferred ^{239}Pu(n,2n) cross section, from Equation (37) at this incident energy, to be low. Figures 9 and 10 display the partial cross sections measured by GEANIE and the ratios calculated by IDA that are used in Equations (36) to (38) to give results in Figure 8.

5.2 The Inferred ^{239}Pu(n,2n) Cross Sections

Further comparisons between the GEANIE data and our calculations indicate that the relative strengths of populating states belonging to different bands are not correctly modeled. While the relative γ-ray intensity, $(8^+ \rightarrow 6^+)/(6^+ \rightarrow 4^+)$, and $(5^- \rightarrow 6^+)/(6^+ \rightarrow 4^+)$, where all states have the lowest energy for the given spin (yrast states), are simulated accurately within experimental error, the population of, for example, the 4^- state, at 1.083 MeV, of the $K = 4$ band with quasiparticle configuration $[\nu 7/2(743) + \nu 1/2(631)]$, is poorly modeled. This can be seen from Figure 11 where the relative γ-ray intensity of $(4^- \rightarrow 4^+)/(6^+ \rightarrow 4^+)$ as a function of incident energy is shown. The theoretical calculation clearly under-predicts the

strength of the population of this 4^- state relative to the 6^+ state of the ground-state band. Similar underestimates are observed for other non-yrast states such as the 1^- state at 0.963 MeV and the 2^- state at 0.968 MeV. Apart from the three reasons given in the previous section, this under-prediction of the population of the non-yrast states could also suggest possible inadequacies in the model prediction of the initial population of the excited states of ^{238}Pu in both excitation energy and angular momentum.

To compensate the tendency of model calculations of overestimating the relative population of the yrast states to non-yrast states, a summing technique is used to infer the final total ^{239}Pu(n,2n) cross section. Specifically, instead of using individual calculated ratios and individual measured partial cross sections to infer the total ^{239}Pu(n,2n) cross section as is done in Equations (36) to (38) and shown in Figure 8, we replace the denominator of Equation (1) by a sum of calculated ratios, $[\sum_i (\mathrm{n}, 2\mathrm{n}\gamma_i)/(\mathrm{n}, 2\mathrm{n})]^{\mathrm{model}}$, of partial to total cross sections. The numerator is replaced by a sum of measured partial cross sections, $[\sum_i (\mathrm{n}, 2\mathrm{n}\gamma_i)]^{\mathrm{experiment}}$ accordingly. The underlying assumption is that for a given initial population of the excited states of ^{238}Pu, which subsequently γ-cascades, the total sum of the γ intensity remains constant regardless of the relative intensities between individual paths through which γ-cascade proceeds. If the (n,2nγ)/(n,2n) ratios corresponding to all independent paths are included in the sum, the incorrect distribution of γ-intensities over various paths could be entirely removed from the inferred total (n,2n) cross section. However, the inference of the ^{239}Pu(n,2n) cross section needs GEANIE data as well as the calculated ratios and only a subset of the independent paths that lead to the ground state of ^{238}Pu are experimentally observed. Specifically, the 7 γ-transitions measured by GEANIE (c.f. Table 10), represent 5 independent γ-decay paths that lead to the ground state of ^{238}Pu. We therefore base our final inference of the ^{239}Pu(n,2n) cross section on a ratio derived from the sum of these 5 transitions. The 5 transitions used are indicated by an asterisk in the last column of Table 10. Furthermore, if the γ-decay from a given state takes several paths and only one is experimentally observed, we include the unobserved decays, as long as they also form independent paths, by multiplying the observed decay by a constant derived from the branching ratios known from other experiments. This situation arises for the $1^- \rightarrow 2^+$ transition. The 1^- state at 0.963 MeV decays to the following states: the 2^+ state at 0.146 MeV, the 0^+ ground state, the 1^- state at 0.605 MeV, and the 3^- state at 0.661 MeV. The relative intensities of its decay to these states are 84, 100, 7.6, and 1.7, respectively. The cross section for the $1^- \rightarrow 2^+$ transition was measured by GEANIE. We include the $1^- \rightarrow 0^+$ and the $1^- \rightarrow 1^-$ decays by multiplying the observed $1^- \rightarrow 2^+$ excitation function by a constant of $2.281 = (84 + 100 + 7.6)/84$. To avoid double counting, the $1^- \rightarrow 3^-$ transition is excluded because all decays from the same 3^- state are included separately in the calculation of the $(3^-/5^- \rightarrow 2^+/4^+)/(\mathrm{n}, 2\mathrm{n})$ ratio, where the transition $3^-/5^- \rightarrow 2^+/4^+$ is a doublet. The final inferred (n,2n)

cross section, ^{239}Pu(n,2n)$^{\text{inferred}}$, is obtained as follows:

$$^{239}\text{Pu(n,2n)}^{\text{inferred}} = \frac{\left\{(6^+\rightarrow 4^+)+(3^-/5^-\rightarrow 2^+/4^+)+(1^-\rightarrow 2^+)\times 2.281+(2^-\rightarrow 2^+)+(4^-\rightarrow 4^+)\right\}^{\text{experiment}}}{\left\{[(6^+\rightarrow 4^+)+(3^-/5^-\rightarrow 2^+/4^+)+(1^-\rightarrow 2^+)\times 2.281+(2^-\rightarrow 2^+)+(4^-\rightarrow 4^+)]/(n,2n)\right\}^{\text{model}}}$$

Figure 12 shows our (GEANIE/IDA) final inferred ^{239}Pu(n,2n) cross section and that inferred from GEANIE/GNASH[1]. For purposes of comparison, measurements by Lougheed near 14 MeV, an Alice[30] calculation by Blann, as well as evaluations from ENDL, ENDF/B-V and ENDF/B-VI are also shown.

The peak value of the our inferred (n,2n) cross section is approximately 327 mb at $E_{\text{inc}} \approx 11.4$ MeV while the peak value from the GEANIE/GNASH inference is immediately below this value. This is much lower than the ENDL and ENDF/B-VI peak value and much higher than the ENDF/B-V evaluation as can be seen from Figure 12. Also seen from the figure is that our inferred (n,2n) cross section agrees very well with Lougheed's measurements near 14 MeV. Beyond $E_{\text{cut}} \approx 14$ MeV, our inferred (n,2n) cross section decreases slower than almost all predictions but the ENDL evaluation. Notice the quite different behaviors of the (n,2n) cross section amongst the previous evaluations almost everywhere within the energy range except around 14 MeV where all evaluations tend to converge to the measurements by Lougheed. We also point out that although in reasonable agreement with calculations by Blann, the two sets of inferred ^{239}Pu(n,2n) cross sections, from IDA and GNASH, are yet again different from all evaluations in terms of how fast the cross section rises around threshold, the peak value, and the general shape of the excitation function. We also note that there are relatively small differences between the two sets of inferred (n,2n) cross sections.

It is seen that, near threshold, the GEANIE/IDA inferred cross section rises faster than all but the ENDF/B-VI evaluation. We should point out that due to the small and yet rapidly changing magnitude of the (n,2n) cross section immediately after the opening of the channel, the modeling of the cross section in this region is very sensitive to the slopes of strong reaction channels such as the reaction cross section and the fission cross section. For example, at $E_{\text{inc}} \approx 5.68$ MeV, a 1.2 % change in fission cross section, which is approximately 20 to 25 mb, would result in a change of about 50 % in the (n,2n) cross section if the difference in fission cross section is mostly propagated into the (n,2n) channel. Furthermore, the subtle competition between the two-neutron emission channel and the weaker γ-emission channel also impacts the shape of the (n,2n) cross section near threshold. To get the correct behavior of the (n,2n) excitation function near threshold is therefore a difficult task, but this will be investigated further. One also notices that the inferred (n,2n) cross section at 5.68 MeV is absent from Figure 12. This is because

[1] All results from GNASH in this report refer to the GNASH00b calculations by Chadwick[6]

the lowest excited state from which a γ-transition is considered in the summed ratio of $[\sum_i (\mathrm{n}, 2\mathrm{n}\gamma_i)/(\mathrm{n}, 2\mathrm{n})]^{\mathrm{model}}$ is the 6^+ state of the ground-state band. The excitation energy of the this state is 0.303 MeV and the (n,2n) channel on this state does not open until $E_{\mathrm{inc}} = 5.95$ MeV. The inferred (n,2n) cross section at the next incident neutron energy point, $E_{\mathrm{inc}} = 6.06$ MeV, would also carry a sizable uncertainty from modeling and it is seen that the experimental uncertainty at this incident energy is also large. We note that the errors on the GEANIE/IDA and GEANIE/GNASH inferred (n,2n) cross section are experimental only.

Our calculations of the 5 individual ratios of ^{239}Pu(n,2nγ)/^{239}Pu(n,2n) as well as their weighted sum, as appears in the equation on page 24, are shown in Figure 13. The corresponding 5 partial cross sections, measured by GEANIE, and their weighted sum are shown in Figure 14. One sees from Figure 13 that the ratio of $(6^+ \rightarrow 4^+)/(\mathrm{n}, 2\mathrm{n})$ is by far the dominant component in the summed ratio. Also noted is that the summed ratio has a smoother behavior between 6 and 7.5 MeV of incident neutron energy than the individual ratio of $(6^+ \rightarrow 4^+)/(\mathrm{n}, 2\mathrm{n})$, primarily due to the inclusion of the ratio of $(3^-/5^- \rightarrow 2^+/4^+)/(\mathrm{n}, 2\mathrm{n})$. We note that all states in these two ratios, namely, the 6^+, 4^+, 3^-, and 5^- states, are members of the yrast band. The strongest transition observed from the non-yrast band is the $4^- \rightarrow 4^+$ transition. In fact, its intensity is only next to the strongest of all transitions observed by GEANIE, namely, the $6^+ \rightarrow 4^+$ transition. Obviously, out of the 5 independent γ-decays, the underestimated population of this 4^- state accounts for the majority of the missing γ's from modeling. Additionally, one sees, by comparing Figure 12 and Figure 8, that the (n,2n) excitation function inferred from the summed partial cross section and the summed ratio has a smoother behavior from threshold to peak, suggesting that the rate of rise of the summed ratio and that of the summed partial cross section data, within this energy region, are comparable. On the other hand, when the rate of rise of the $(6^+ \rightarrow 4^+)/(\mathrm{n}, 2\mathrm{n})$ ratio and that of the $6^+ \rightarrow 4^+$ partial cross section data are compared, the slight slowing down of the rise in the $6^+ \rightarrow 4^+$ partial cross section between 8 and approximately 10 MeV (c.f. Figure 9) causes the inferred (n,2n) cross section from this particular ratio to dip in this energy interval (c.f. Figure 8).

5.3 Sensitivity of the ^{239}Pu(n,2nγ)/^{239}Pu(n,2n) to the Angular Momentum Dependence of the Fission Barriers

The physical models and input parameters impact the outcome of the calculations. In this section, we discuss the sensitivity of the model calculations of the ratios, ^{239}Pu(n,2nγ)/^{239}Pu(n,2n), primarily to the angular momentum dependence of the fission barriers.

Focusing on the ratios of ^{239}Pu(n,2nγ)/^{239}Pu(n,2n), which are what the model calculations are tasked to provide, there are two areas in which sensitivity studies should be emphasized. One is the initial population of the excited states in the

residual nucleus, ^{238}Pu, as a function of excitation energy and angular momentum; the other is the subsequent γ-cascade mechanism for a given initial population. We have discussed the latter in Section 4.3 with an emphasis on the discrete spectroscopy. We showed the impact of the discrete spectroscopy in the ^{238}Pu nucleus on the calculated relative γ-transition intensities in Figures 6 and 7. Apart from the details of the spectroscopy for a given $E_{\rm cut}$, earlier calculations[31] of ^{235}U(n,2n) cross sections also pointed out that the choice of $E_{\rm cut}$ has a large effect on the (n,2nγ)/(n,2n) ratios.

The initial population of the excited states in ^{238}Pu as a function of excitation energy and angular momentum is determined, mainly, by the strength and spin dependence of the preequilibrium and compound reactions. The latter includes particle emission, fission, and γ-decay. The choice of optical model potential parameters has a smaller effect on the initial energy distribution in ^{238}Pu through its effect on the strength of the direct inelastic scattering cross section. However, studies carried out earlier[32] suggest that the difference in the ratio of ^{239}Pu(n,2n$\gamma^{6^+\rightarrow 4^+}$)/^{239}Pu(n,2n) between a spherical optical model potential and a deformed one is at most about 8 %. This earlier study also showed that the difference made to the ^{239}Pu(n,2n$\gamma^{6^+\rightarrow 4^+}$)/^{239}Pu(n,2n) ratio by the two deformed optical model potentials, one from Dietrich which is the model used in the current calculations, and the other from Madland, is less than 3 %. As discussed in Section 3, the strength of the preequilibrium emission in our current calculations is determined by comparing the calculated neutron emission spectrum with that measured by Kammerdiener. As for the spin dependence associated with the preequilibrium emissions, the effects on the angular momentum distribution in the residual nucleus due to different spin transfer mechanisms remain to be studied. In this section, we focus on the effect of the angular momentum dependence of the fission barriers on the final calculated ratios of ^{239}Pu(n,2nγ)/^{239}Pu(n,2n).

The dependence of the fission barrier V on the angular momentum J of the fissioning system in Equation (23) is made so that the faster the nucleus spins, the easier it is for the system to undergo fission. When this angular momentum dependence is turned off, the dependence of the fission transmission coefficient on angular momentum comes solely from the level density as can be seen from Equation (23). Often, the non-angular-momentum-dependent fission barrier is used in modeling various reaction cross sections for actinides, as is the case in the GNASH calculations shown in Figure 12. To see, quantitatively, how this angular momentum dependence impacts various ratios of ^{239}Pu(n,2nγ)/^{239}Pu(n,2n), we carried out calculations both with and without the dependence of V on J. The two fission barriers in each fissioning nucleus are assumed to have the same dependence on J. Results are shown in Figure 15. The red curves are various ratios calculated when the angular momentum dependence of the fission barrier is turned on whereas the black curves are the same calculated ratios when that dependence is turned off. In both cases, the fission parameters are tuned so that the calculated fission

cross section fits the ENDL99 and JENDL3.3 evaluations as shown in Figure 4. It can be seen that by turning on the angular momentum dependence of the fission barriers, the dominant ratio, namely, $(6^+ \rightarrow 4^+)/(\mathrm{n}, 2\mathrm{n})$, is lowered by about 6 %. The largest change in this ratio occurs around the (n,2n) threshold and beyond, roughly, 10 MeV. The changes to the other ratios are much smaller and the dependence of V on J can raise the ratios as well as decrease them. However, the net effect on the summed ratio is that the dependence of V on J lowers the summed ratio around threshold by about 10 % to 15 % and it lowers the summed ratio by about 4 % after 10 MeV of incident neutron energy. In terms of the inferred (n,2n) cross section, turning off the dependence of V on J would lower the inferred (n,2n) cross section around threshold by about 11 % to 17 % and it would lower the inferred (n,2n) cross section beyond, roughly, 10 MeV by about 4 %. Comparing the inferred (n,2n) cross sections from IDA and GNASH (c.f. Figure 12), one can conclude that one of the reasons that the inferred (n,2n) cross section from GNASH is lower, particularly around threshold and at higher energies, could be the absence of the dependence of V on J. We learn from this sensitivity study that the angular momentum dependence of the fission barriers does impact the ratios of ^{239}Pu(n,2nγ)/^{239}Pu(n,2n) as it affects the spin distribution in the residual nucleus, ^{238}Pu, and the effect appears to be significant around the (n,2n) threshold region. The higher the angular momentum of the state from which γ-decay originates, the more pronounced the effect on the ratio of ^{239}Pu(n,2nγ)/^{239}Pu(n,2n), in accord with the assumption that the higher the angular momentum, the more the lowering of the fission barrier height.

Another physical quantity that affects the spin distribution in various nuclei is the spin cut-off parameter in the level density. Calculations for the n + ^{235}U reaction, where better quality and more extensive data are available, are carried out with two sets of spin cut-off parameters for the Fermi-gas level density formula for both neutron-emission and fission channels. They are: $\sigma^2(E^*) = 0.0888A^{2/3}\sqrt{aE^*}$ and $\sigma^2(E^*) = 0.146A^{2/3}\sqrt{aE^*}$. The former leads to an excellent reproduction of the GEANIE measurements of the relative populations of various discrete states in ^{234}U. We therefore adopted it in the calculations for the n + ^{239}Pu reaction. Incidentally, the spin cut-off parameter formula of $\sigma^2(E^*) = 0.0888A^{2/3}\sqrt{aE^*}$ is also used in the GNASH calculations.

5.4 Uncertainties

The largest uncertainty, from both experimental measurements and theoretical calculations, in the inferred (n,2n) cross section is around the threshold region. The theoretical uncertainties of the calculated summed ratio are difficult to quantify due to the number of physics models involved and the number of parameters in each of these models. However, independent model calculations do provide an estimate of the variation of theoretical predictions. In Figure 12, the ^{239}Pu(n,2n) cross

section inferred from both IDA and GNASH calculations, based on the same set of GEANIE data are shown. Although they do differ, especially around threshold and in the high incident-neutron-energy region, the fact that the two independent calculations agree with each other within experimental error is nevertheless remarkable. The averaged difference between the two sets of inferred (n,2n) cross sections is less than 15 %. Another independent calculation is being carried out at LLNL using the nuclear reaction modeling code STAPRE. Upon detailed comparisons, we find differences in intermediate results between the three codes, in particular, between the IDA calculations and that from GNASH and STAPRE. Despite the modeling differences which need to be further studied, preliminary calculations from STAPRE show close agreement for the inferred ^{239}Pu(n,2n) cross sections with IDA around the threshold region, and close agreement with GNASH in the high energy tail of the excitation function. The convergence of the inferred ^{239}Pu(n,2n) cross sections from all three modeling codes leads us to conclude that the uncertainty from the theoretical calculations is such that the final inferred ^{239}Pu(n,2n) excitation function, as shown in Figure 12, is correct to within, probably, 15 %.

6 Conclusions

We have successfully calculated the ratios of ^{239}Pu(n,2nγ)/^{239}Pu(n,2n) and subsequently obtained inferred ^{239}Pu(n,2n) cross sections between 5.68 and 17.18 MeV incident neutron energy. Our inferred ^{239}Pu(n,2n) cross section peaks at $E_{\rm inc} \approx 11.4$ with a peak value of approximately 326 mb. This new ^{239}Pu(n,2n) excitation function is much different in shape from all previous evaluations and its peak cross section differs from the previous evaluations by as much as 40 %. At $E_{\rm inc} \approx 14$ MeV, our ^{239}Pu(n,2n) cross section is found to be in good agreement with the radio-chemical measurements by Lougheed. Comparisons between the inferred (n,2n) cross sections derived from GEANIE/IDA and GEANIE/GNASH show strong convergence to the final excitation function presented in Figure 12 in spite of the existing differences in details between the different calculations.

The extended level scheme we generated for ^{238}Pu leads to improvements to the relative γ-ray intensities of $(8^+ \rightarrow 6^+)/(6^+ \rightarrow 4^+)$ and $(5^- \rightarrow 6^+)/(6^+ \rightarrow 4^+)$ by about 25 % and 35 %, respectively, as shown in Figure 6 and 7. The dependence of the fission barrier height on angular momentum is found to lower the summed ratio (c.f equation on page 24) mostly near the threshold region and above 10 MeV. As a consequence, the inclusion of the angular momentum dependence of the fission barrier height increases the inferred ^{239}Pu(n,2n) cross section by about 11 % to 17 % near threshold and by about 4 % beyond 10 MeV. Finally, the use of the summed ratio, $[\sum_i (\mathrm{n}, 2\mathrm{n}\gamma_i)/(\mathrm{n}, 2\mathrm{n})]^{\rm model}$, and the summed partial cross sections, $[\sum_i (\mathrm{n}, 2\mathrm{n}\gamma_i)]^{\rm experiment}$, in the inference of the final ^{239}Pu(n,2n) cross section results in good agreement between our inferred (n,2n) cross sections and that measured by Lougheed. It clearly reduced the bias of modeling to overestimate the population

of yrast states and leads to inferred ^{239}Pu(n,2n) cross sections that are consistent between GEANIE/IDA and GEANIE/GNASH within experimental errors.

7 Acknowledgment

The authors wish to acknowledge useful discussions with John A. Becker, Lee A. Bernstein, and Dennis McNabb. Important earlier contributions to this work[32] from Alan M. Ross, Gianni Reffo, and Roger M. White are also acknowledged.

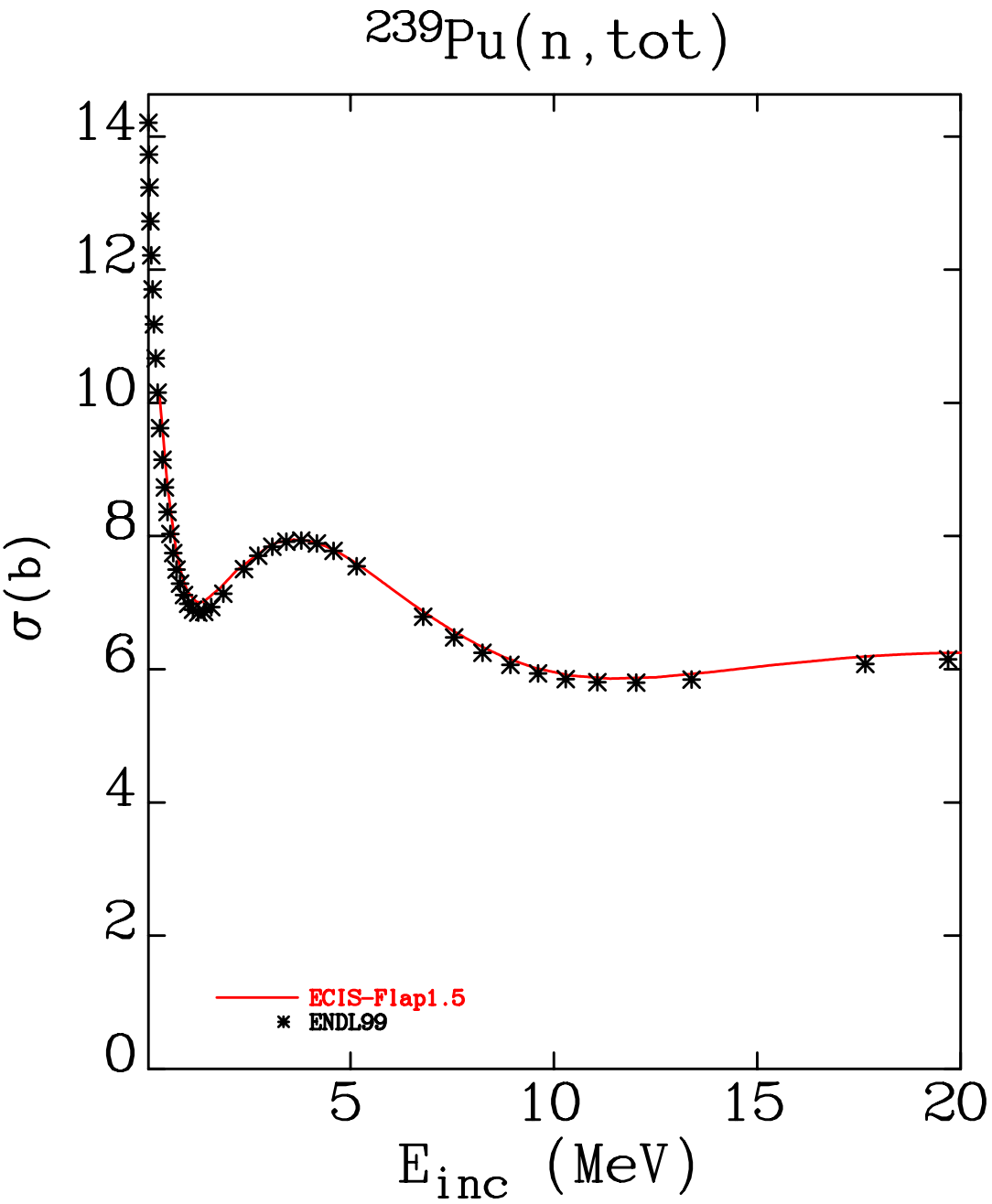

Figure 1: *n + ^{239}Pu total cross section as a function of incident neutron energy. Solid line represents a 5 coupled-channel calculation by ECIS using the optical model potential Flap1.5. Symbols give the ENDL99 evaluation.*

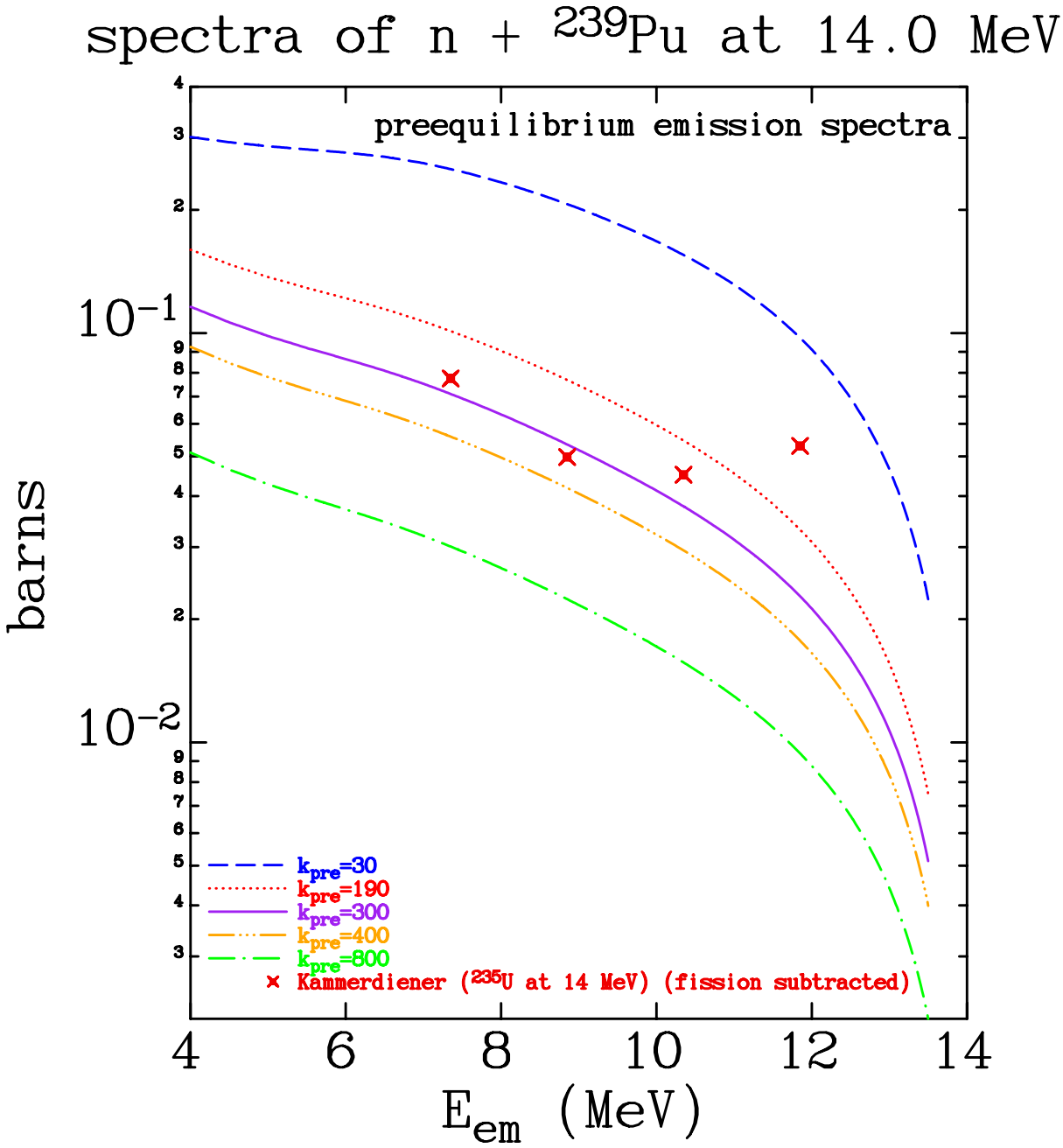

Figure 2: *Preequilibrium neutron emission spectra of* $n + {}^{239}Pu$ *at* 14 *MeV calculated from IDA with various strengths of* M^2*, and neutron emission spectrum of* $n + {}^{235}U$ *at* 14 *MeV measured by Kammerdiener.*

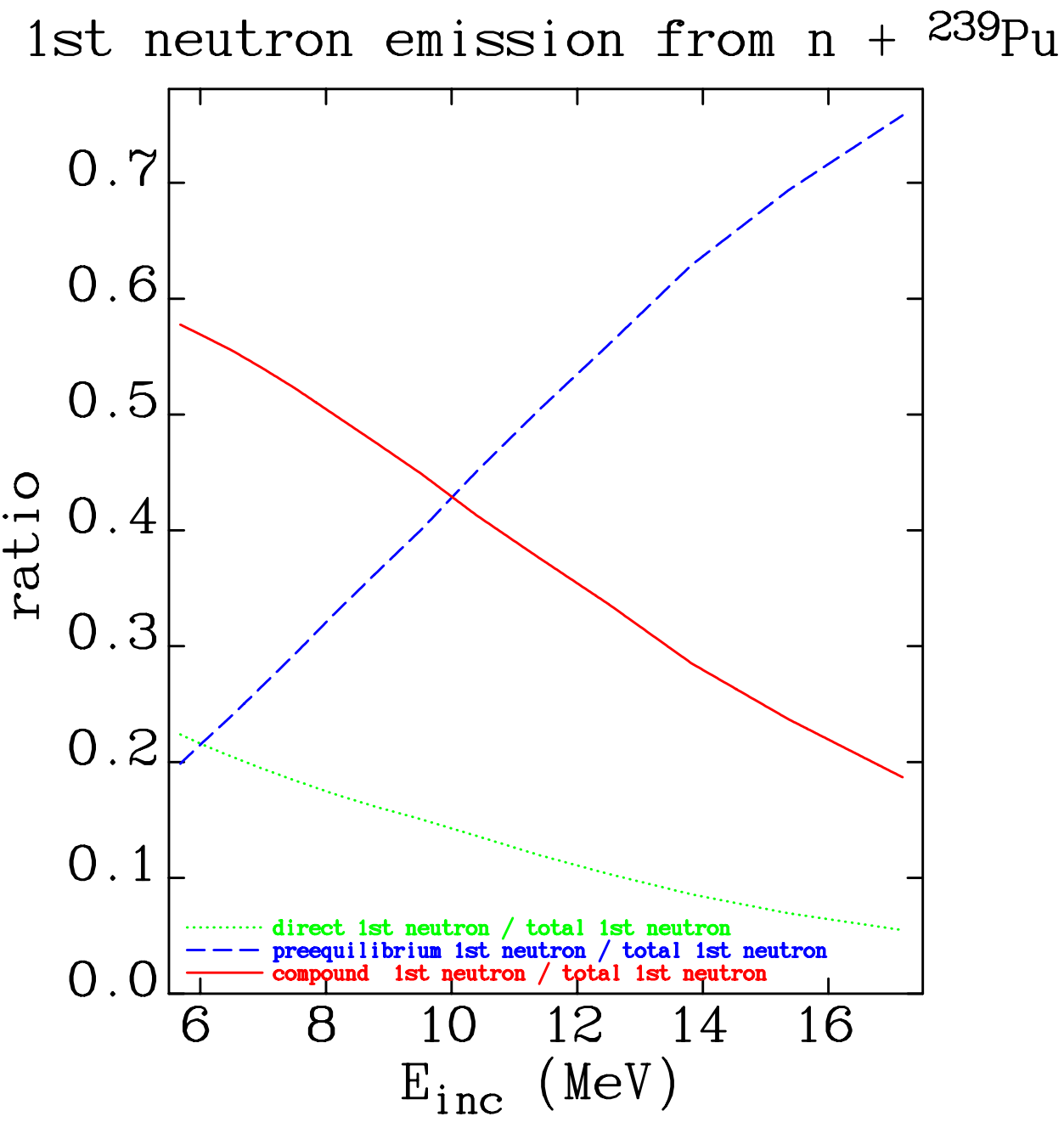

Figure 3: *Ratios of the cross section of the first neutron emitted via the direct, preequilibrium, and compound mechanisms, respectively, over the cross section of total first neutron emission, as a function of incident neutron energy.*

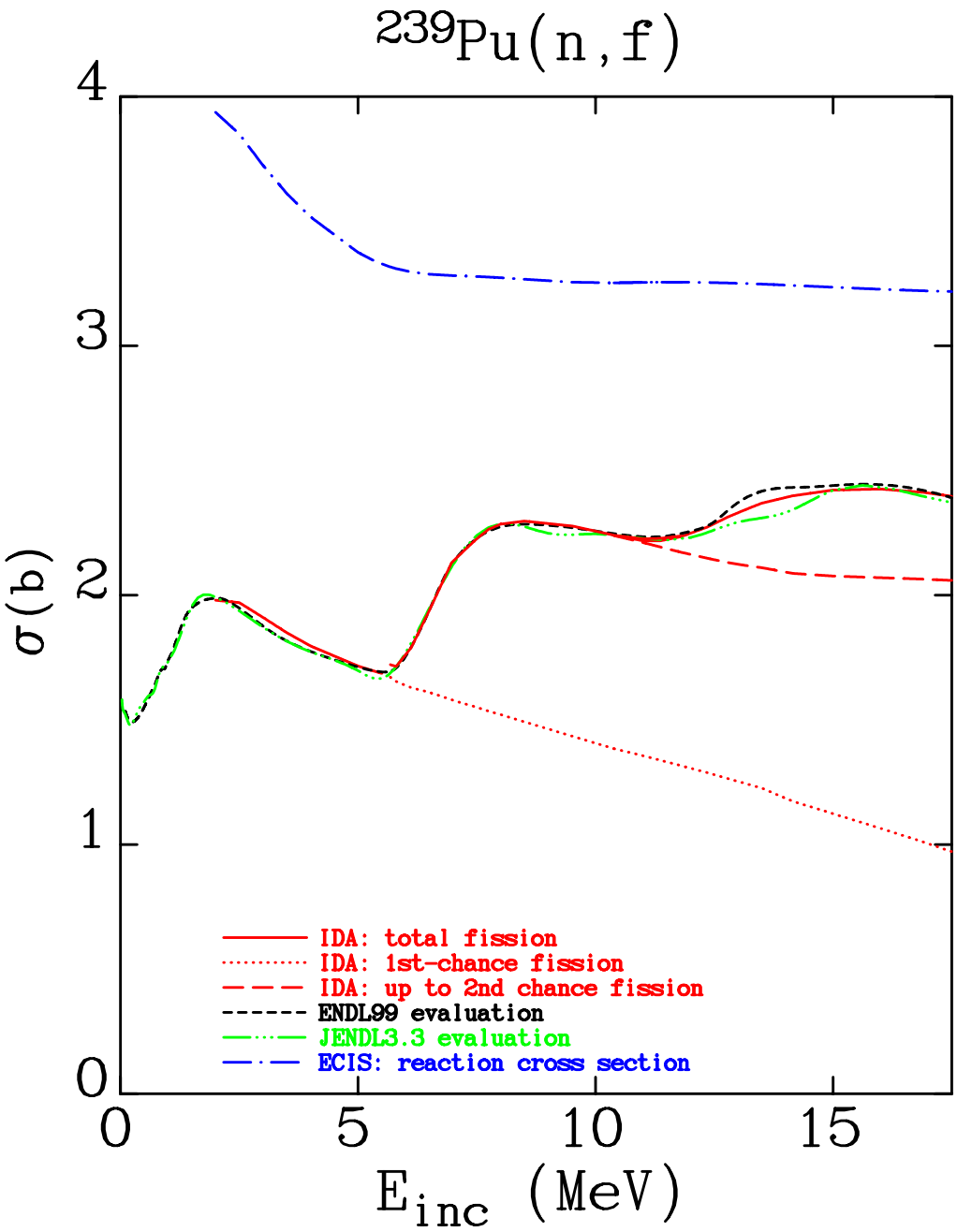

Figure 4: *The $^{239}Pu(n,f)$ cross section, as a function of $E_{\rm inc}$, calculated from IDA and its evaluations from ENDL99[10] and JENDL3.3[23]. The top curve is the reaction cross section, $\sigma_{\rm R}$, calculated from ECIS as a function of $E_{\rm inc}$.*

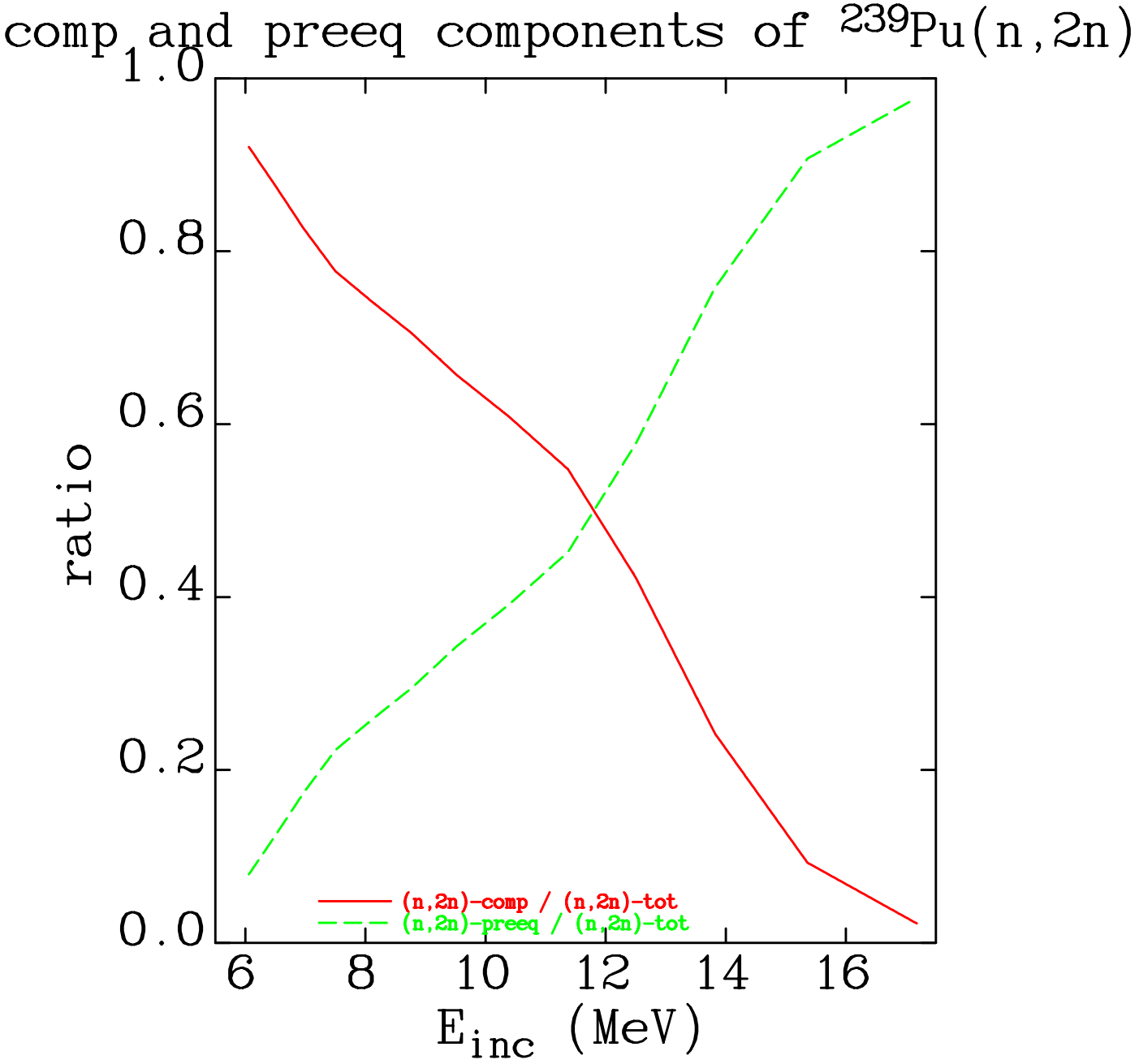

Figure 5: *Fractions of the compound and preequilibrium components of the (n,2n) cross section to the total (n,2n) cross section as a function of* $E_{\rm inc}$ *calculated from IDA. In the preequilibrium component of (n,2n) cross section, only the first neutron is emitted via the preequilibrium mechanism.*

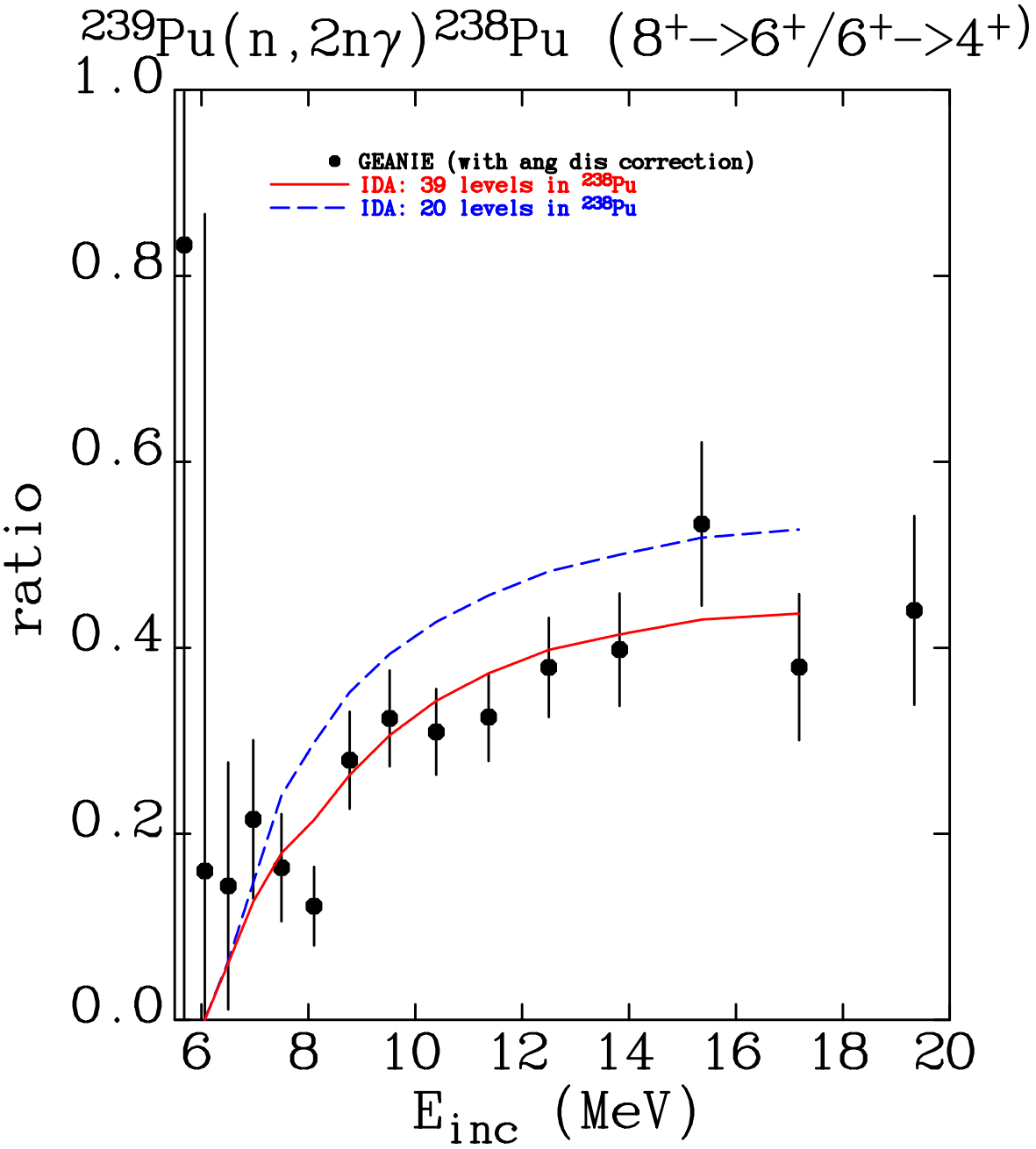

Figure 6: *Relative γ-ray intensity of* $(8^+ \rightarrow 6^+)/(6^+ \rightarrow 4^+)$ *calculated by IDA and measured by GEANIE. Two separate calculations are carried out. One uses 20 discrete levels of* ^{238}*Pu obtained from ENSDF. The other employs our extended level scheme of* ^{238}*Pu with 39 levels, discussed in the text. States* 8^+, 6^+, *and* 4^+ *all belong to the ground-state band with excitation energies of* 0.513, 0.303, *and* 0.146 *MeV, respectively.*

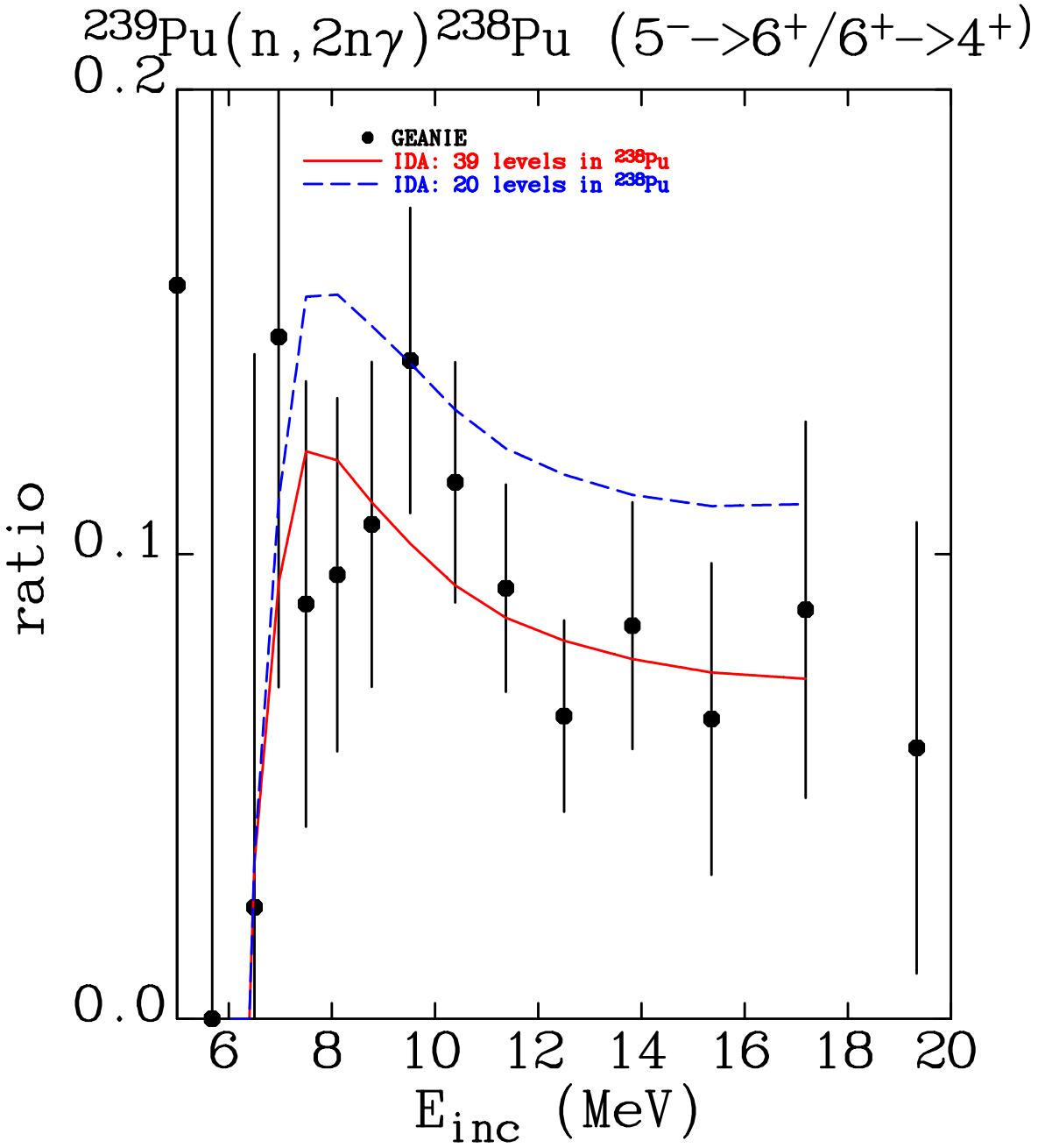

Figure 7: *Relative γ-ray intensity of $(5^- \rightarrow 6^+)/(6^+ \rightarrow 4^+)$ calculated by IDA and measured by GEANIE. Two separate calculations are carried out. One uses 20 discrete levels of ^{238}Pu obtained from ENSDF. The other employs our extended level scheme of ^{238}Pu with 39 levels, discussed in the text. States 6^+ and 4^+ belong to the ground-state band with excitation energies of 0.303 MeV and 0.146 MeV, respectively. State 5^- at 0.763 MeV of excitation energy belongs to the octupole band.*

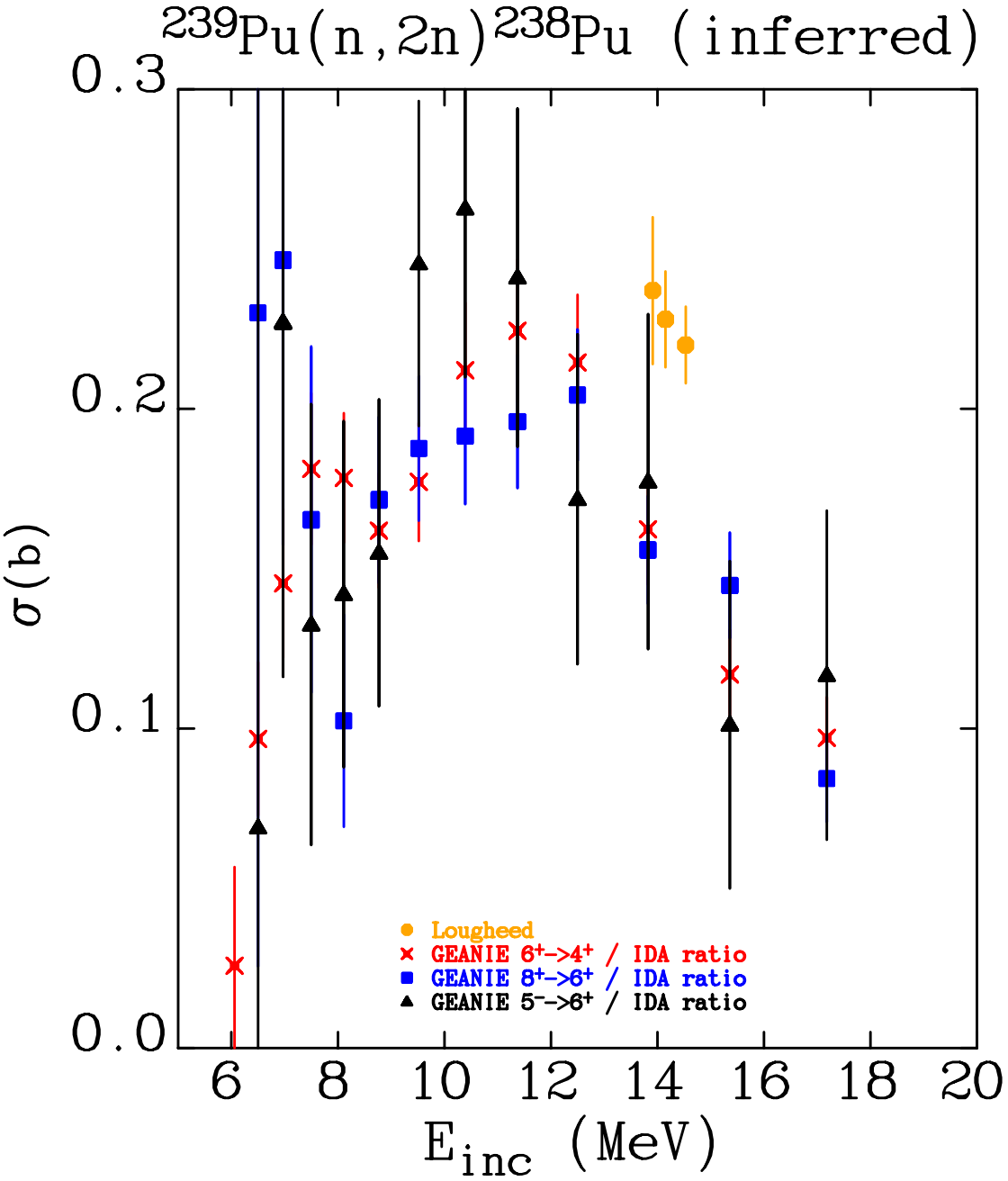

Figure 8: *Inferred* $^{239}Pu(n,2n)$ *cross sections, according to Equations (36) to (38), using our calculated ratios of* $^{239}Pu(n,2n\gamma)/^{239}Pu(n,2n)$ *and GEANIE data. Measurements by Lougheed near* 14 *MeV are also shown.*

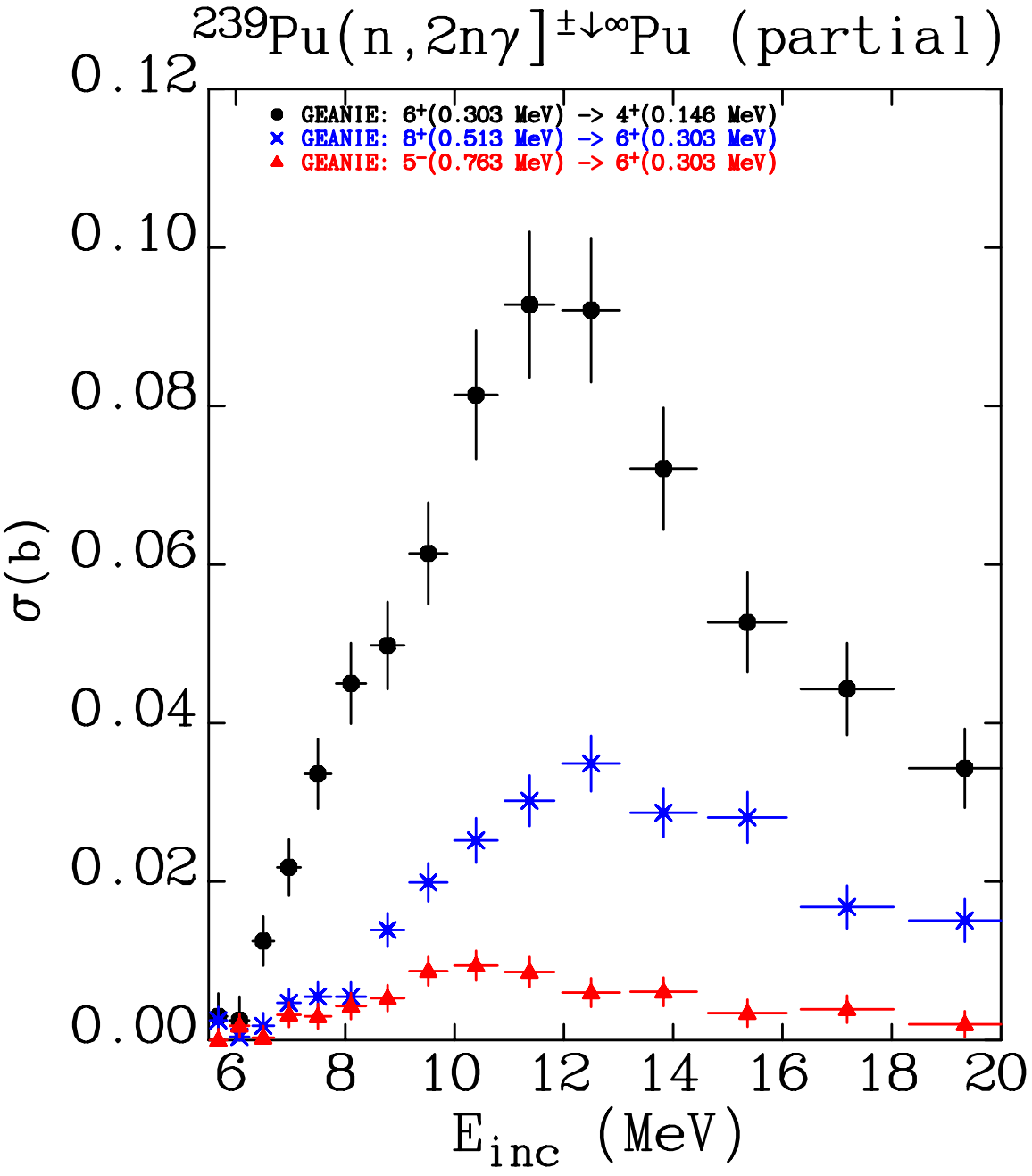

Figure 9: *Partial cross section* $^{239}Pu(n,2n\gamma)^{238}Pu$ *measurements for the* $6^+ \rightarrow 4^+$, $8^+ \rightarrow 6^+$, *and* $5^- \rightarrow 6^+$ *tansitions obtained from GEANIE.*

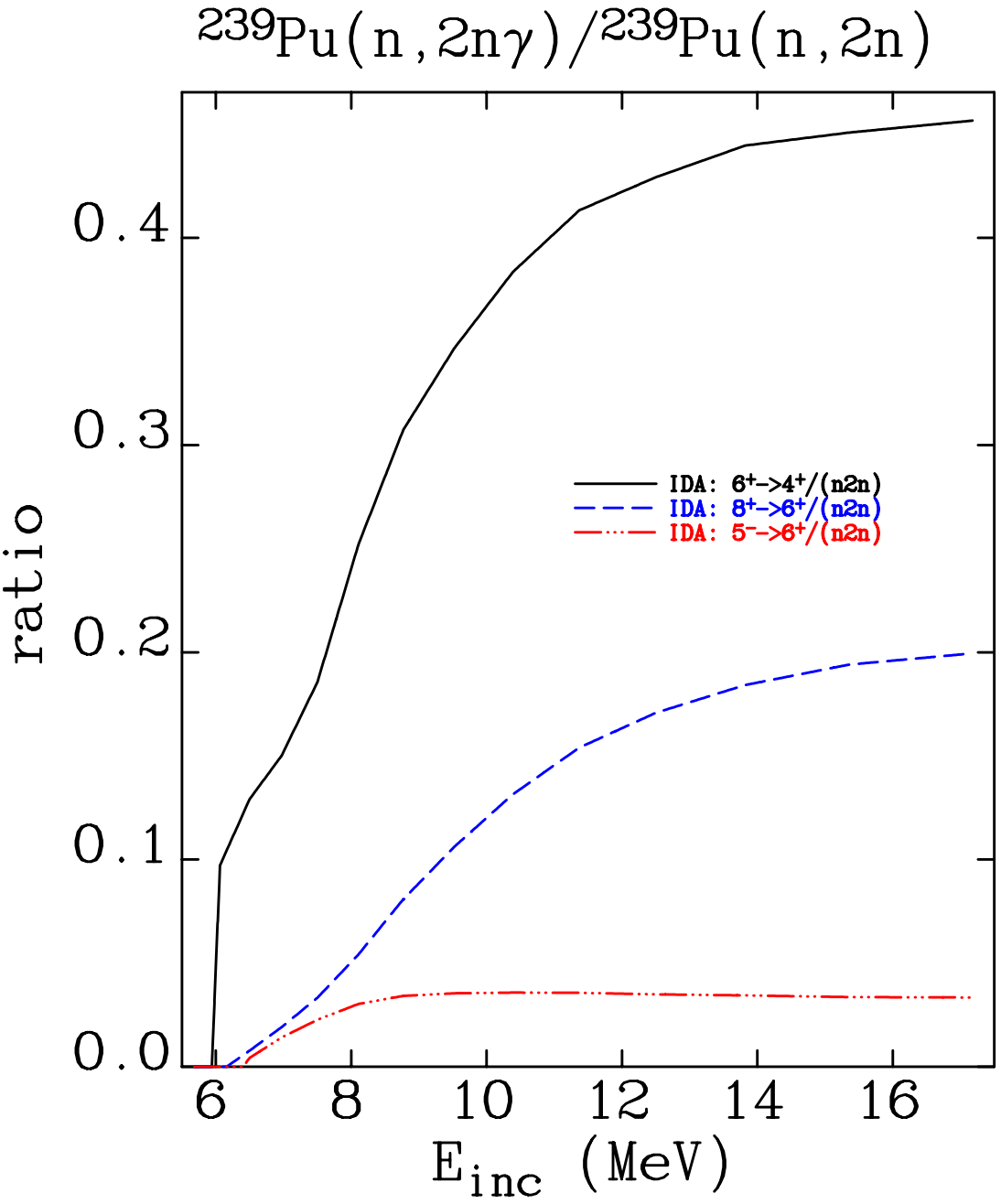

Figure 10: *Calculated ratios of* $^{239}Pu(n,2n\gamma^{6^+\to4^+})/^{239}Pu(n,2n)$, $^{239}Pu(n,2n\gamma^{8^+\to6^+})/^{239}Pu(n,2n)$, *and* $^{239}Pu(n,2n\gamma^{5^-\to6^+})/^{239}Pu(n,2n)$.

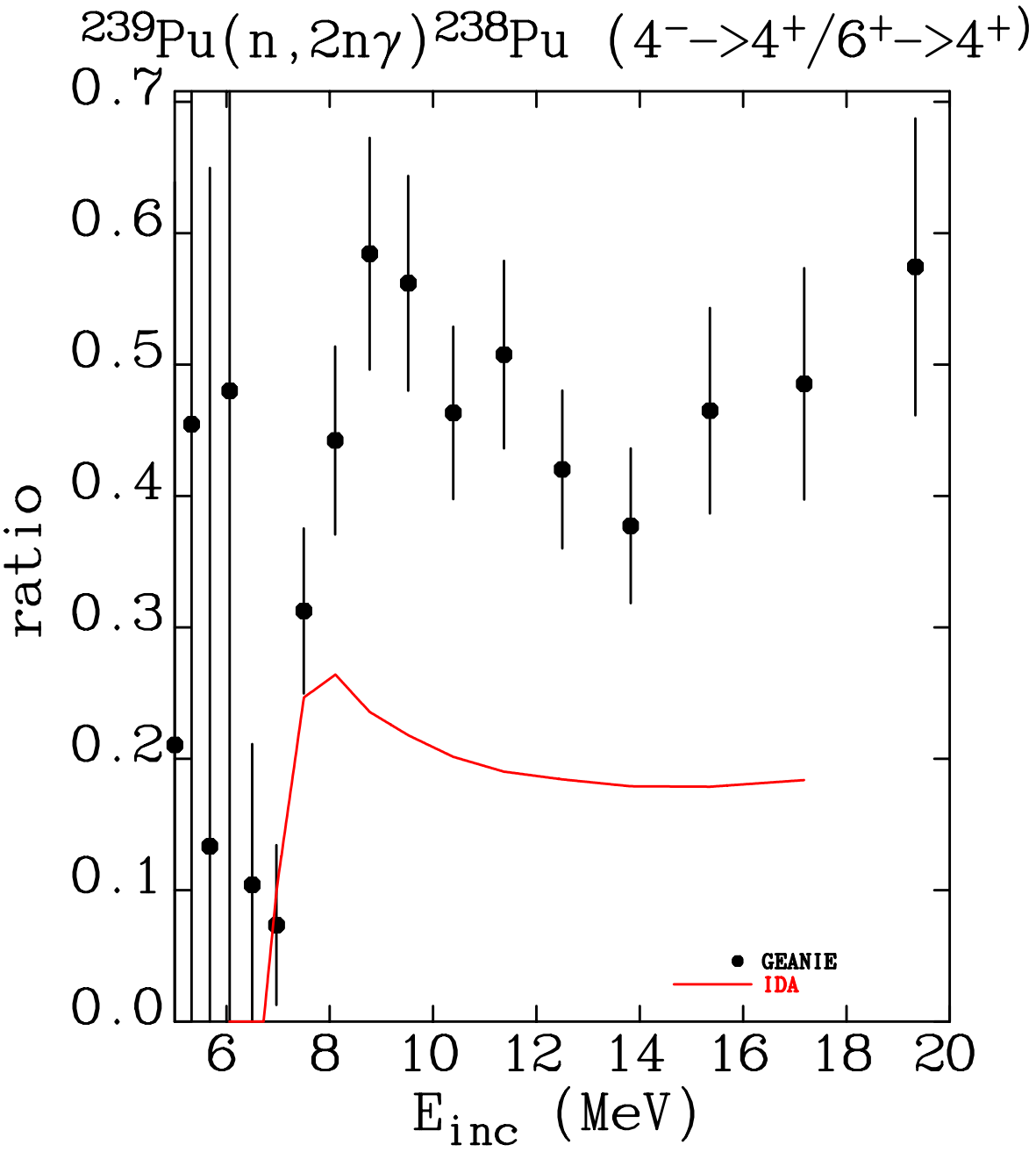

Figure 11: *Relative γ-ray intensity of $(4^- \rightarrow 4^+)/(6^+ \rightarrow 4^+)$ as a function of incident neutron energy, measured by GEANIE and calculated by IDA. The 4^- state has an excitation energy of* 1.083 *MeV and belongs to the $K = 4$ band of the ^{238}Pu nucleus.*

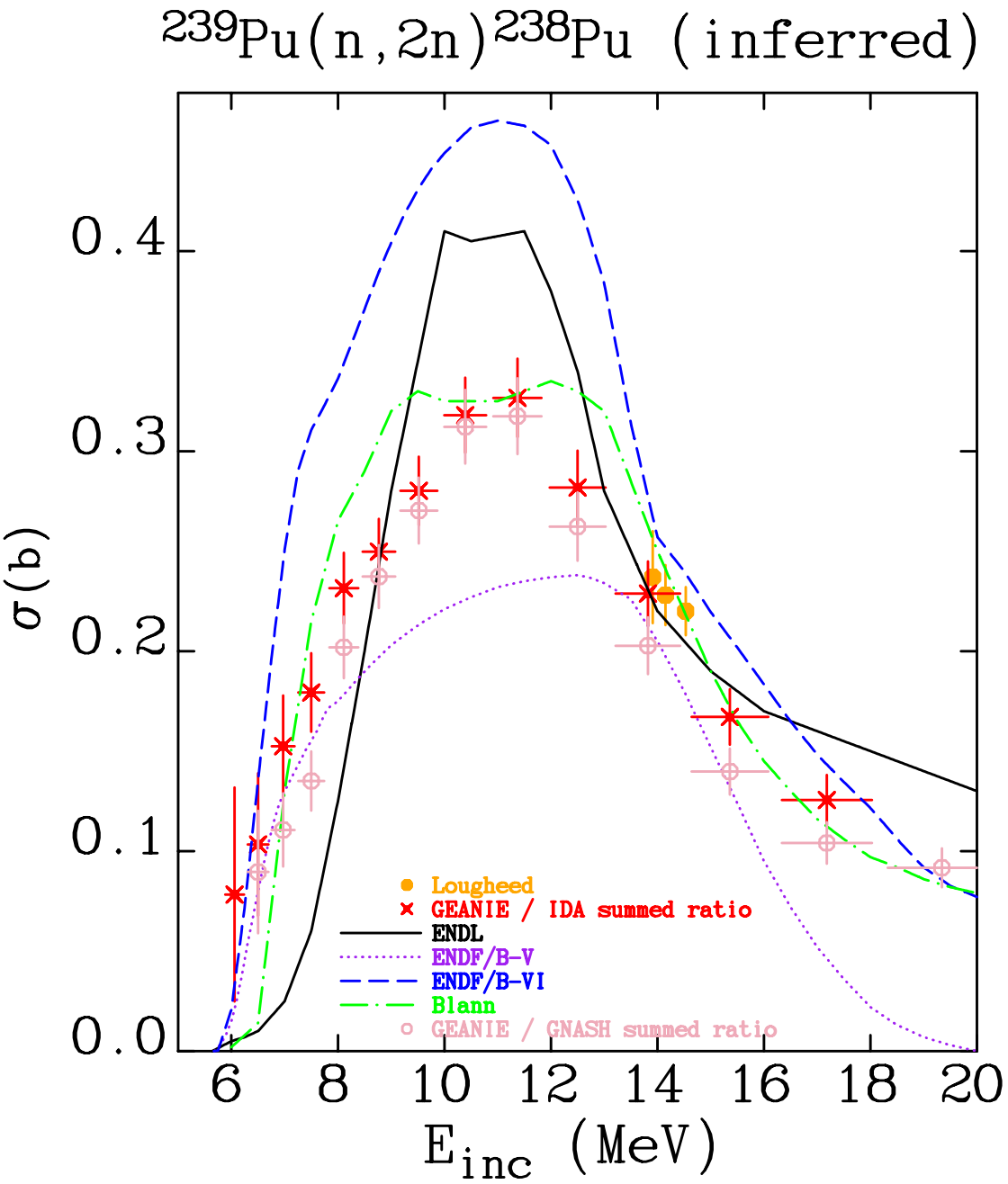

Figure 12: *Final inferred $^{239}Pu(n,2n)$ cross section as a function of incident neutron energy using GEANIE data and IDA calculations from the equation on page 24.*

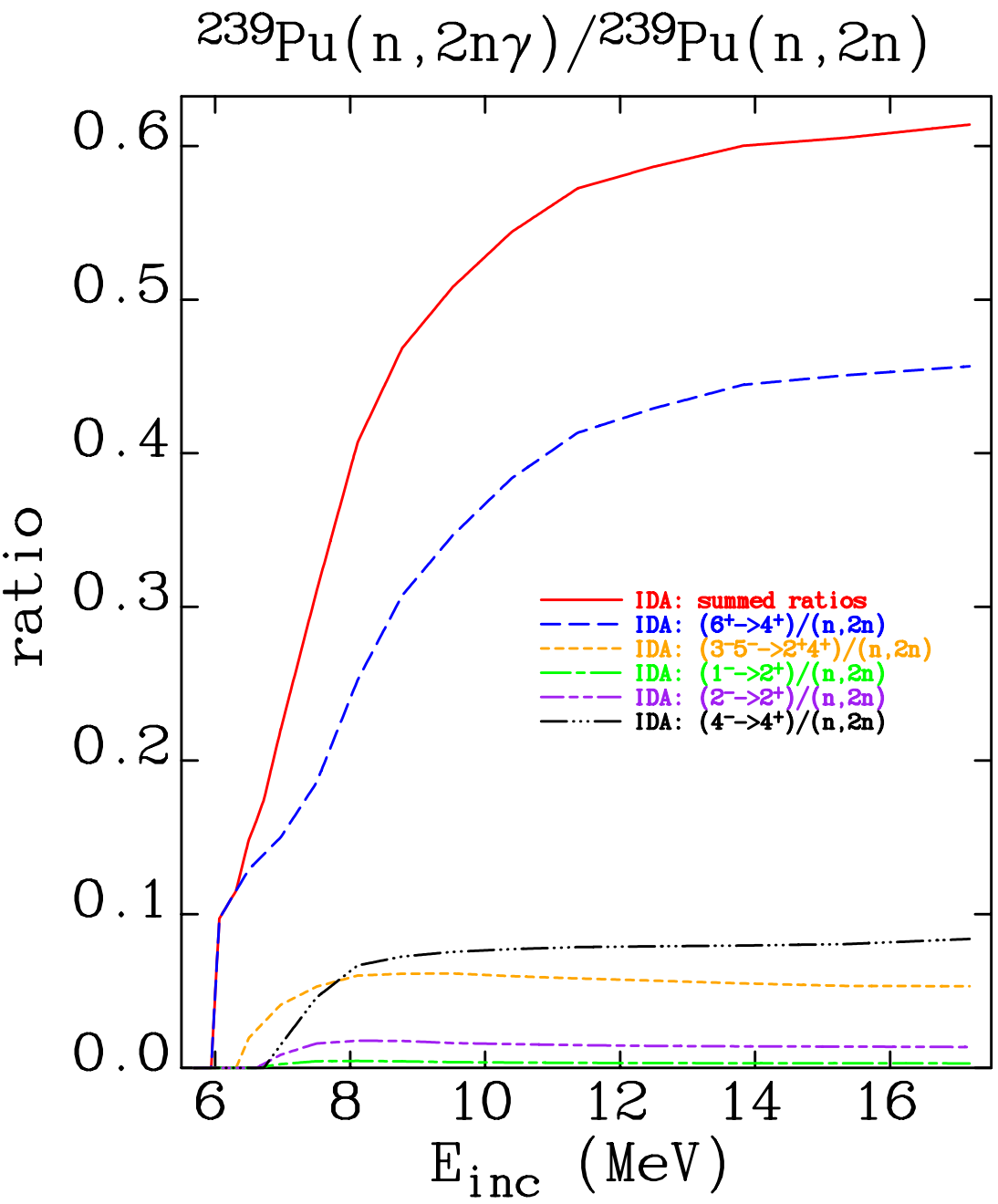

Figure 13: *Ratios of* $(6^+ \rightarrow 4^+)/(n,2n)$, $(3^-/5^- \rightarrow 2^+/4^+)/(n,2n)$, $(1^- \rightarrow 2^+)/(n,2n)$, $(2^- \rightarrow 2^+)/(n,2n)$, *and* $(4^- \rightarrow 4^+)/(n,2n)$ *as well as their weighted sum, as defined in the equation on page 24, as a function of incident neutron energy, calculated by IDA.*

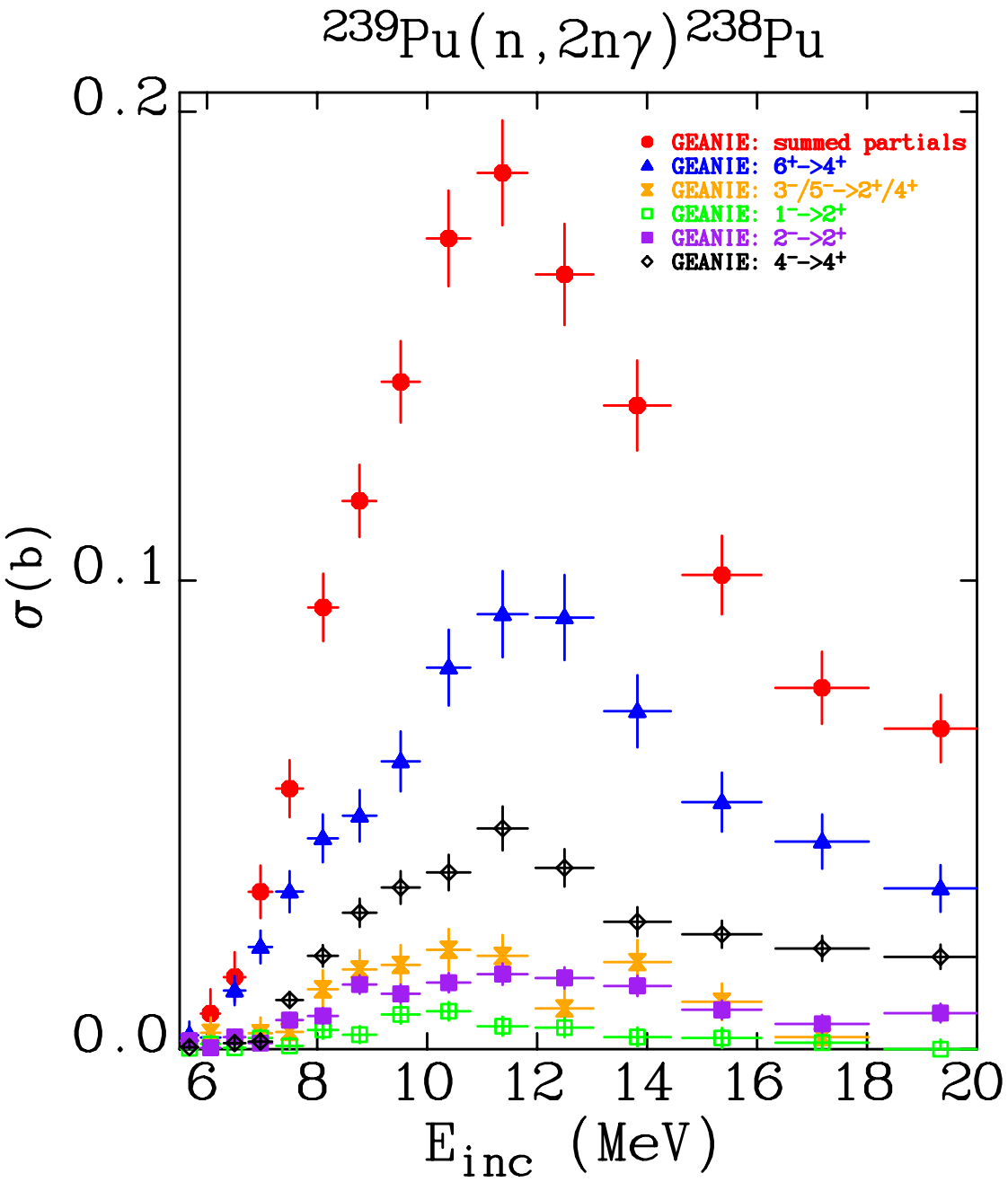

Figure 14: *Partial* $^{239}Pu(n,2n\gamma)$ *cross sections for the transitions of* $(6^+ \rightarrow 4^+)$, $(3^-/5^- \rightarrow 2^+/4^+)$, $(1^- \rightarrow 2^+)$, $(2^- \rightarrow 2^+)$, *and* $(4^- \rightarrow 4^+)$ *as well as their weighted sum, as defined in the equation on page 24, as a function of incident neutron energy, measured by GEANIE.*

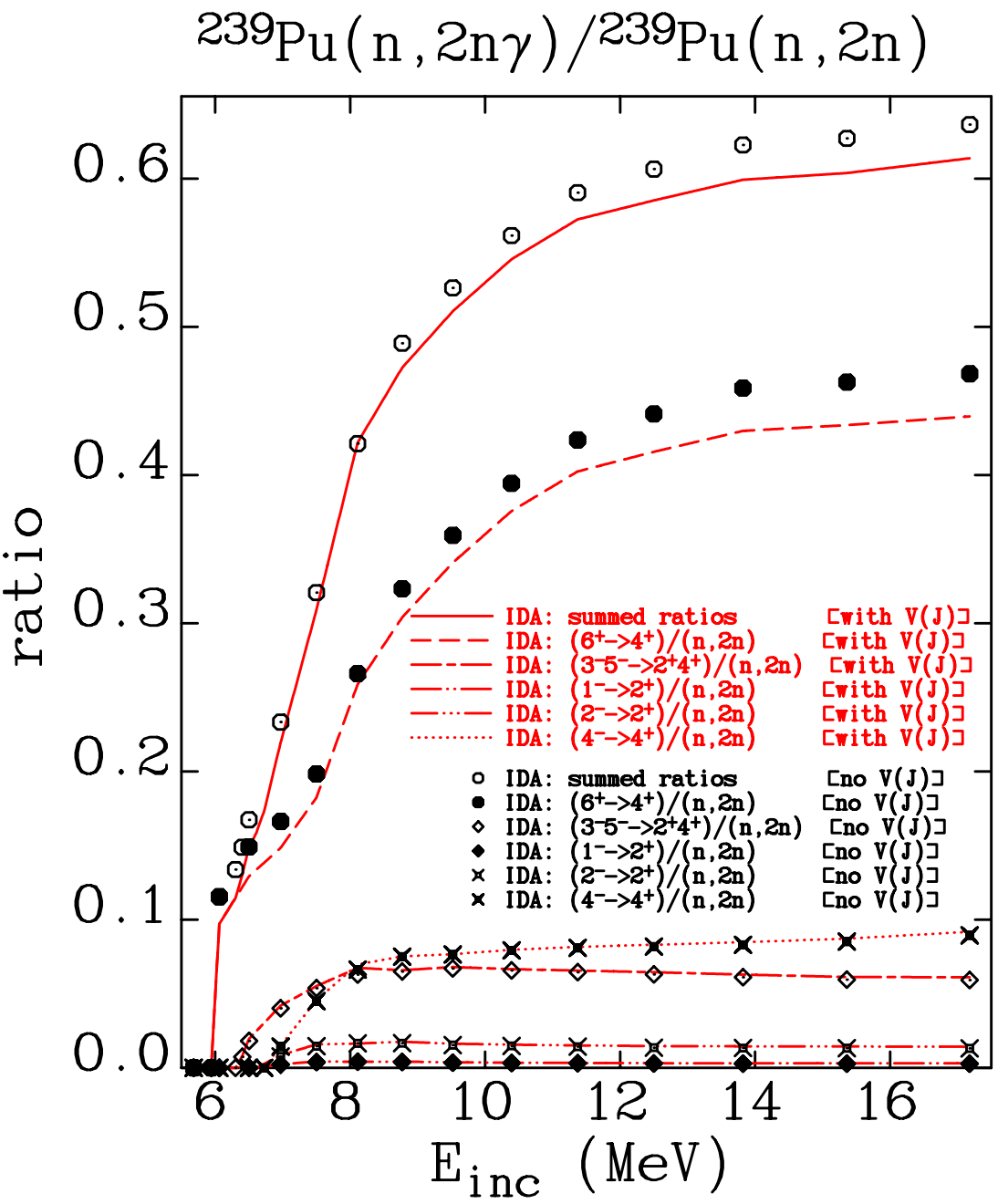

Figure 15: *Ratios of* $(6^+ \rightarrow 4^+)/(n,2n)$, $(3^-/5^- \rightarrow 2^+/4^+)/(n,2n)$, $(1^- \rightarrow 2^+)/(n,2n)$, $(2^- \rightarrow 2^+)/(n,2n)$, *and* $(4^- \rightarrow 4^+)/(n,2n)$ *as well as their weighted sum, as defined in the equation on page 24, calculated by IDA with and without angular momentum dependence of the fission barriers.*

References

[1] J. Frehaut, "Proceedings of International conference on Nuclear Data for Basic and Applied Science", Santa Fe, p1561, edited by P. Young, R. Brown, G. Auchampaugh, P. Lisowski, and L. Stewart. Gordon and Breach Science Publishers, (1985).

[2] D.S. Mather *et al.*, "Measurement of (n,2n) Cross Sections for Incident Energies between 6 and 14 MeV", AWRE Report N. 072/72 (1972).

[3] R. Lougheed, Lawrence Livermore National Laboratory, private communication.

[4] J.A. Becker and M.B. Chadwick, "Measurement of the ^{239}Pu(n,2n) Cross Section between Threshold and 15 MeV", Project Proposal, (1995).

[5] G. Reffo and F. Fabbri, IDA system of codes, unpublished.

[6] M.B. Chadwick, private communication, (2000).

[7] P.E. Hodgson, "The Optical Model of Elastic Scattering", Oxford University Press, (1963).

[8] F.S. Dietrich, J.P. Delaroche, J. Rapaport, and D. Madland, a manuscript on optical model to be published.

[9] J. Raynal, code ECIS95, unpublished.

[10] M.A. Ross, H. Chen, E. Ormand, and R.M. White, "A New LLNL Evaluation of Neutron Induced Reactions on ^{239}Pu", report in preparation, Lawrence Livermore National Laboratory, (2000).

[11] J.M. Akkermans, H. Gruppelaar, and G. Reffo, *Phys. Rev. C* **22**, 73(1980).

[12] P.G. Young, E.D. Arthur, and M.B. Chadwick, "Comprehensive Nuclear Model Calculations: Introduction to the Theory and Use of the GNASH Code", LA-**12343**-MS, (UC-413), Los Alamos National Laboratory, (1992); LA-UR-**96-3739**, (1996).

[13] F.C. Williams, *Nucl. Phys.* **A166**, 231(1971).

[14] C. Kalbach-Cline, *Nucl. Phys.* **A120**, 590(1973).

[15] J.L. Kammerdiener, "Neutron Spectra Emitted by ^{239}Pu, ^{238}U, ^{235}U, Pb, Nb, Ni, Al, and C Irradiated by 14 MeV Neutrons", Ph.D thesis, (1972).

[16] P. Rose, "ENDF-201: ENDF/B Summary Documentation", Fourth Edition (ENDF/B-VI), Brookhaven National Laboratory report, BNL-NCS-**17541**, (1992).

[17] W. Hauser and H. Feshbach, *Phys. Rev.* **87**, 366(1952).

[18] E. Vogt, "The Statistical Theory of Nuclear Reactions", *Adv. Nucl. Phys.* Vol **1**, Chapter 4, Plenum Press, NY., (1968).

[19] S.E. Bjornholm and J.E. Lynn, "The Double-Humped Fission Barrier", *Rev. Mod. Phys.*, **52**, 725(1980).

[20] D.L. Hill and J.A. Wheeler, *Rev. Mod. Phys.*, **89**, 1102(1953).

[21] A.J. Sierk, private communication.

[22] A. Gilbert and A.G.W Cameron, *Canadian Journal of Physics*, **43**, 1446(1965).

[23] T. Kawano, H. Matsunobu, T. Murata, A. Zukeran, Y. Nakajima, M. Kawai, O. Iwamoto, K. Shibata, T. Nakagawa, T. Ohsawa, M. Baba, and T. Yoshida, "Evaluation of Fission Cross Sections and Covariances for ^{233}U, ^{235}U, ^{238}U,^{239}Pu, ^{240}Pu, and ^{241}Pu", JAERI-Research, 2000-004, (2000).

[24] J.K. Tuli, "Evaluated Nuclear Structure Data File - A Manual for Preparation of Data Sets", Brookhaven National Laboratory, (1987).

[25] G. Reffo, "Parameter Systematics for Statistical Theory Calculations of Neutron Reaction Cross Sections", IAEA(UNESCO) Winter Courses in Nuclear Physics and Reactors, January 17 - March 10, 1978, Trieste. IAEA-SMR-43 (1980).

[26] E. Gadioli and P.E. Hodgson, "Pre-Equilibrium Nuclear Reactions", Clarendon Press, Oxford, (1992).

[27] G.A Bartholomew, E.D. Earle, A.J. Ferguson, J.W. Knowles, and M.A. Lone, "Gamma-Ray Strength Functions", *Adv. Nucl. Phys.* Vol **7**, Chapter 4, Plenum Press, N.Y., (1974).

[28] D.M. Brink, *D. Phil. Thesis*, University of Oxford, (1955).

[29] P. Axel, *Phys. Rev.*, **126**, 671(1962).

[30] M. Blann, private communication.

[31] H. Chen, M.A. Ross, G. Reffo, R.M. White, and W. Younes, "A Preliminary Calculation of ^{235}U(n,2n)^{234}U Cross Sections", UCRL-ID-**137718**, Lawrence Livermore National Laboratory, (1999).

[32] M.A. Ross, H. Chen, G. Reffo and R.M. White, "The ^{239}Pu$(n, 2n)^{238}$Pu Cross Section: Preliminary Calculations", UCRL-ID-**133497**, Lawrence Livermore National Laboratory, (1999).